Basic Principles of White Dwarf Asteroseismology

G. Fontaine[1], P. Brassard[1], S. Charpinet[2], P.-O. Quirion[3], S.K. Randall[4], and V. Van Grootel[5]

[1]Département de Physique, Université de Montréal, Montréal, Québec, Canada H3C 3J7
[2]Laboratoire d'Astrophysique de Toulouse-Tarbes, Université de Toulouse, CNRS, 14 av. E. Belin, 31400 Toulouse, France
[3]Institut for Fysik og Astronomi, Aarhus Universitet, Aarhus, Denmark DK-8000
[4]European Southern Observatory, Karl-Schwarzschild-Str. 2, 85748 Garching bei München, Germany
[5]Institut d'Astrophysique et de Géophysique, Université de Liège, Allée du 6 août 17, B4000 Liège, Belgium

1 Asteroseismology and White Dwarf Stars

The technique of asteroseismology exploits the information contained in the normal modes of vibration that may be excited during particular phases in the evolution of a star. Such modes modulate the emergent flux of a pulsating star and manifest themselves primarily in terms of multiperiodic luminosity variations. In its simplest form, observational asteroseismology consists in gathering light curves, i.e., monitoring the (variable) brightness of pulsating stars as a function of time. Standard signal processing methods, such as Fourier techniques for example, are then used to extract the periods (or, equivalently, frequencies), the apparent amplitudes, and the relative phases of the detected pulsation modes.

The next step – in essence the most basic component of the asteroseismological approach as a whole – consists in comparing the observed pulsation periods with periods computed from stellar models with the hope of finding an optimal model that provides a good physical description of the real pulsating star under scrutiny. To insure that the search for the optimal model in parameter space is done objectively and automatically requires good model-building capabilities, efficient period-matching algorithms, and considerable computing power. Otherwise, with simpler trial-and-error search methods, there always remains a doubt about the uniqueness and validity of the best period-matching model that comes out of the exercise, a weakness that has plagued most of asteroseismology so far.

The periods of pulsation modes of stellar models can generally be computed quite accurately and reliably within the framework of the linear theory of stellar pulsations in its adiabatic version (see below). The same framework (although complementary nonadiabatic calculations are then necessary) may be used to compute first-order corrections to the unperturbed emergent flux, an approach that is fundamental in the exploitation of the additional information contained in the observed amplitudes and relative phases of the detected pulsation modes. And indeed, constraints on the angular geometry of a given observed pulsation mode may be obtained by comparing theoretical amplitude ratios and phase differences with those observed in different wavebands through multicolor photometry and/or time-resolved spectroscopy. The same is true when exploiting the relative amplitudes of modes in a given waveband in conjunction with those of their harmonics and cross-frequency components in the Fourier domain. When available, such inferences on the angular geometry of pulsation modes may provide extremely valuable constraints in the search for the optimal model in parameter space. In the end, if successful, an asteroseismological exercise leads to the determination of the global structural parameters of a pulsating star and provides unique information on its internal structure and evolutionary state. An outstanding example of such a successful exercise is that provided recently by [11] for the pulsating sdB component of the close eclipsing binary system PG 1336−018.

The technique of asteroseismology has found particularly fertile grounds at the bottom of the HR diagram where several distinct types of pulsating stars have been discovered. These are generally referred to as the compact pulsators (i.e., those with surface gravities $\log g \gtrsim 5$). Figure 1 illustrates that portion of the surface gravity-effective temperature plane where these families are found. Those include the ZZ Ceti stars which are H-atmosphere white dwarfs with $T_{\rm eff} \simeq 12{,}000$ K (first discovered by [26]), the V777 Her stars which are He-atmosphere white dwarfs with $T_{\rm eff} \simeq 25{,}000$ K ([45]), and the GW Vir pulsators which are He/C/O-atmosphere white dwarfs with $T_{\rm eff} \simeq 120{,}000$ K ([28]). Figure 1 also indicates the locations of two other categories of pulsators which were discovered more recently. These are the V361 Hya stars which are short-period pulsating hot B subdwarf (sdB) stars ([24]), and the long-period V1093 Her pulsators which are cooler and less compact sdB stars ([21]). In addition, short-period pulsations have also been reported in the, so far, unique object SDSS J1600+0748 ([46]), a very hot sdO subdwarf with $\log g \sim 5.9$ and $T_{\rm eff} \sim 71{,}000$ K ([19]). This object may or may not be related to a group of four sdO subdwarfs found in the cluster ω Cen, and clustered around $T_{\rm eff} \sim 50{,}000$ K, for which pulsational instabilities were recently discovered ([35]). Moreover, [30] have found the presence of at least one pulsation mode in SDSS J1426+5752, a member of an entirely new and unexpected kind of very rare white dwarfs, those of the so-called Hot DQ spectral type, which are relatively cool ($T_{\rm eff} \simeq 20{,}000$ K) stars with atmospheres dominated by carbon ([13]). At the time of this writing, four more pulsating Hot DQ white dwarfs have been found (see, e.g., [14]). In all cases, the pulsators that we

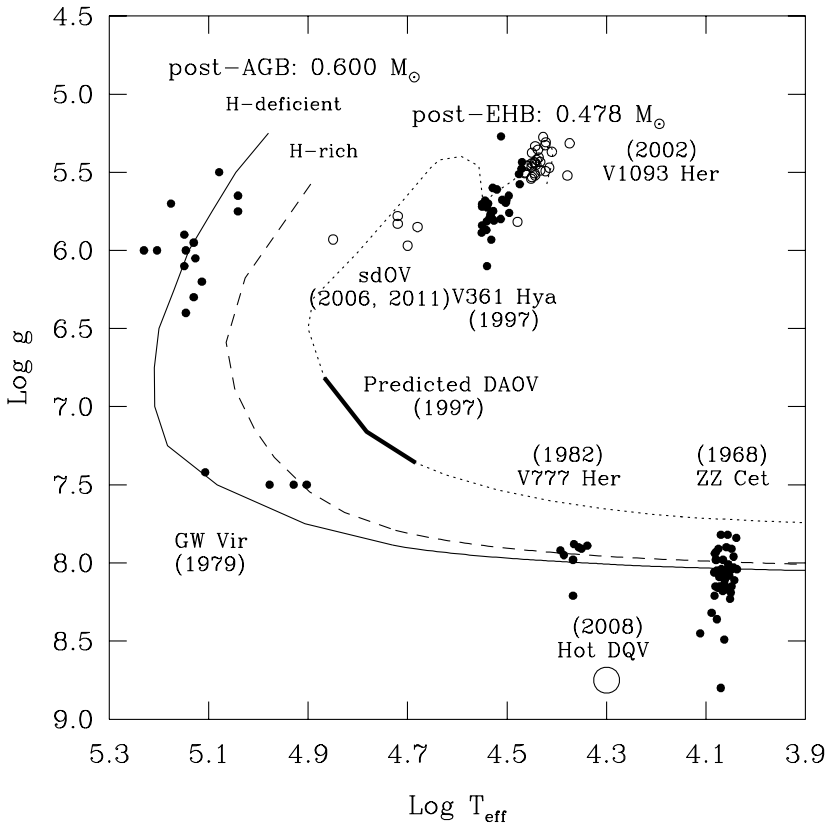

Fig. 1. Region of the log g−log $T_{\rm eff}$ plane where the compact pulsators are found. Each of five distinct families is identified by its official IAU name, and the year of the report of the discovery of the prototype of each class is also indicated. Two more categories are identified by the year of their discovery, 2006−2011 and 2008, respectively. Typical evolutionary tracks are plotted showing 1) the track followed by a 0.6 $M_{\odot}$ post-AGB, H-rich star which becomes a H-atmosphere white dwarf (dashed curve), 2) the path followed by a 0.6 $M_{\odot}$ post-AGB, H-deficient star which becomes a He-atmosphere white dwarf (solid curve), and 3) the path followed by a 0.478 $M_{\odot}$ post-EHB model which leads to the formation of a low-mass H-atmosphere white dwarf (dotted curve).

refer to are isolated stars or components of non-interacting binaries, and their luminosity variations are caused by internal partial ionization mechanisms. For completeness, we further point out that pulsational instabilities have also been discovered in several accreting white dwarfs in cataclysmic variables ([43]; [1] and references therein).

In the rest of this paper, we focus exclusively on the four kinds of isolated pulsating white dwarfs that we currently know of. Representative light curves,

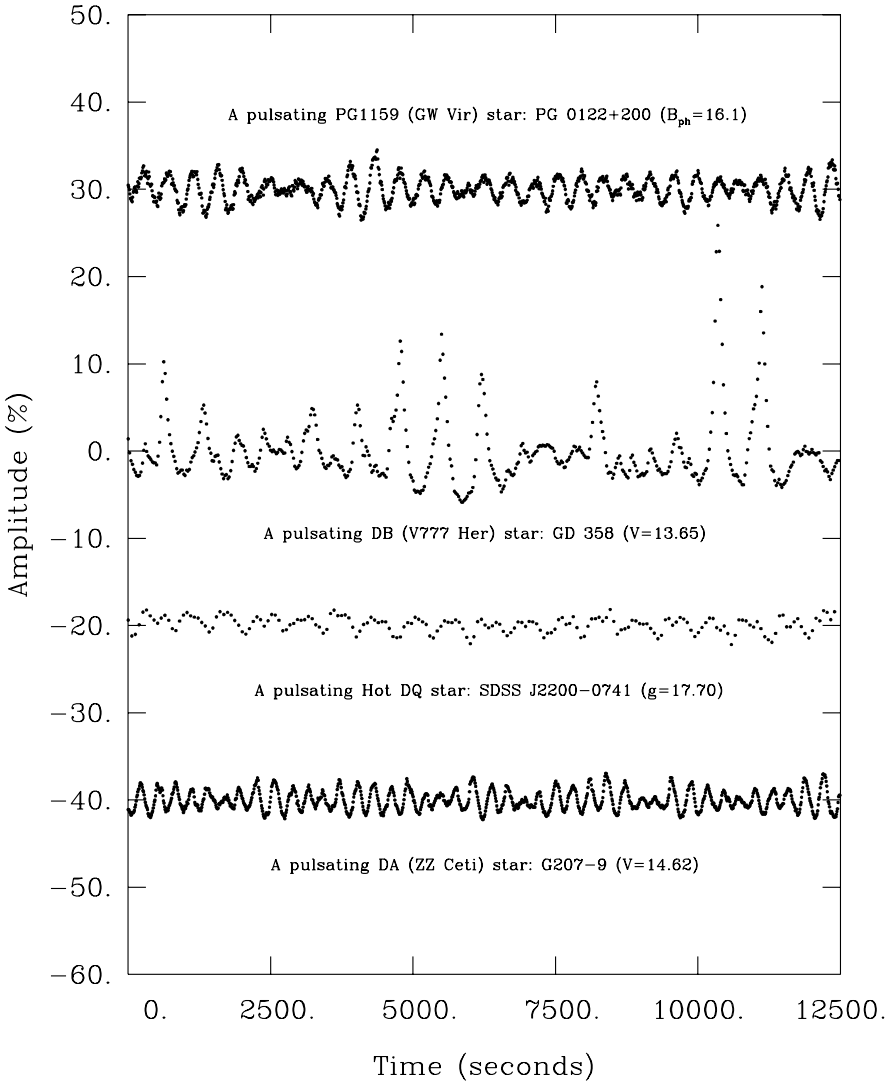

Fig. 2. Segments of typical optical light curves for each of the four known types of isolated pulsating white dwarfs. The curves referring to PG 0122+200, GD 358, and G207−9 were obtained with LAPOUNE, the Montréal portable 3-channel photometer attached to the 3.6 m CFHT telescope. This photometer uses photomultiplier tubes as detectors. No filter was used, so these are integrated "white light" data. In comparison, the curve for the much fainter star SDSS J2200−0741 was obtained by Betsy Green and Patrick Dufour using the Mont4K CCD camera mounted on the Steward Observatory 1.6 m Kuiper telescope through a Schott 8612 broadband filter.

one each for each of the different kinds, are shown in Figure 2. They are typical in that they all show multiperiodic variations and a clear tendency to exhibit increasingly nonlinear behavior with increasing amplitude (as exemplified by the case of the large-amplitude pulsating DB white dwarf GD 358 shown here). Pulsating white dwarfs generally have light curves that show peak-to-peak amplitudes in the range from $\sim$0.4 millimag in the lowest amplitude pulsators known to upward of 0.3 mag in the largest amplitude ones. The luminosity variations are due to the presence of low-degree (l=1 and l=2) and low- to medium-order gravity modes that are excited through a partial ionization mechanism (see below). The observed periods generally lie in the range from about 100 s to some 1400 s, although the upper limit can extend to several thousand seconds in low-gravity GW Vir pulsators.

The properties of the pulsating white dwarfs have been extensively reviewed recently by [17] and we refer the reader to that paper for the relevant details. In addition, [44] have provided another review on these stars. Given the availability of those papers, we felt that it would be more useful to discuss the topic from another point of view rather than provide what would necessarily amount to a shortened version of those manuscripts. Hence, in a pedagogical spirit, we decided to use our allocated space to present a discussion of the principles underlying the theory of pulsating stars as applied to white dwarfs. Our target audience is therefore researchers not necessarily familiar with pulsation theory and those that are but may not be well-acquainted with the peculiarities of white dwarf physics.

2 Normal Modes of Vibration in a Homogeneous Continuous Elastic Medium

It is useful to first recall some elementary physics concerning normal modes of vibration in simple mechanical systems. Thus, under the specific assumption that the displacements of matter have small amplitudes compared to the dimensions of the system (this is the realm of the *linear approach*), the spatial and temporal behaviors of perturbations in a homogeneous elastic medium are governed by the classical wave equation,

$$\frac{\partial^2 \boldsymbol{\psi}\left(\boldsymbol{r},t\right)}{\partial t^2} = \frac{\sigma(k)^2}{k^2}\nabla^2 \boldsymbol{\psi}\left(\boldsymbol{r},t\right), \tag{1}$$

where $\boldsymbol{\psi}\left(\boldsymbol{r},t\right)$ is, in general, a continuous function of space and time. This wave function could represent, for example, the (small) displacement of an element of matter with respect to its equilibrium position. In this equation, $\sigma(k)$ is the angular frequency and k is the wave number.

The general solution to this equation corresponds to an acoustic or sound wave which propagates with a speed $c = \sigma/k$, a constant characteristic of the specific elastic medium of interest. In an infinite medium, a continuum of frequencies is allowed, $0 \leq \sigma \leq \infty$, in principle. For finite dimensions, however,

there are boundary conditions to be respected at the frontiers of the domain, where waves are reflected. Only the waves with the "correct" wavelength or frequency (generally those with a node or an extremum at the boundaries) will resonate, the others disappearing through destructive interference after several reflections. The normal modes of vibration are the solutions of the classical wave equation in presence of boundary conditions (which transform the problem into an eigenvalue problem). Only certain solutions are allowed (the normal modes or eigenfunctions), corresponding to a discrete spectrum of possible values of the angular oscillation frequency (the eigenvalues $\sigma_0 < \sigma_1 < \sigma_2, ...$). In a normal mode, all moving parts oscillate at the same frequency and go through their equilibrium positions at the same time.

As a specific example, consider the simple case of the transverse oscillations of an ideal elastic rectangular membrane of dimension $X \times Y$ that is attached at the edges. In that case, the wave function is a simple scalar, $\psi(x, y, t)$, and the appropriate boundary conditions are specified by $\psi(x = 0, y, t) = \psi(x = X, y, t) = \psi(x, y = 0, t) = \psi(x, y = Y, t) = 0$. The solution of the classical wave equation for this simple problem is well known. Specifically, the eigenfunctions are given by,

$$\psi(x, y, t) \sim sin(k_{n_x} x) sin(k_{n_y} y) e^{i\sigma_{n_x, n_y} t}. \tag{2}$$

Note that the amplitude remains undefined (as in any linear problem) and is usually normalized to some convenient arbitrary constant. Likewise, the eigenvalues are given by,

$$\sigma_{n_x, n_y} = c\sqrt{k_{n_x}^2 + k_{n_y}^2}, \tag{3}$$

where c is the (constant) speed of sound, and

$$k_{n_x} = (n_x + 1)\frac{\pi}{X}, \quad n_x = 0, 1, 2, ..., \quad \text{and} \quad k_{n_y} = (n_y + 1)\frac{\pi}{Y}, \quad n_y = 0, 1, 2, ... \tag{4}$$

Hence, in our 2D system, there are 2 "quantum" numbers , n_x and n_y, to specify a mode. These numbers correspond, respectively, to the number of nodal lines that cut the x and y axis. Note that if there are symmetries (e.g., a square membrane), then different modes may have the same oscillation frequency. Such modes are called degenerate modes. It is easy to infer that an eigenmode in 3D should be specified by three quantum numbers representing the number of nodal *surfaces* that cut across the system. Furthermore, if there are symmetries such as that found in a spherical model of a star, then degenerate eigenmodes are automatically present.

3 Normal Modes of Vibration in Stars

Stars are not homogeneous systems. They can be generally considered, in a first approximation, as self-gravitating fluid spheres with a depth-dependent

chemical composition. The speed of sound is not uniform (it depends on depth) and, furthermore, the fluid elements in a star are subjected to a variable gravitational acceleration from $g = 0$ at the center to $g = g_s$ at the surface. The waves that propagate inside a star are no longer pure acoustic (or sound) waves, but they are of the gravito-acoustic type. Such waves are subjected to specific boundary conditions at the center and at the surface of the star. The waves are reflected there and one often speaks of a gravito-acoustic cavity to describe a star in relation to its normal modes of vibration.

In its most basic form (see, in this context, the excellent textbook by [40]), the linear theory of nonradial stellar oscillations uses as a starting point three well-known hydrodynamic equations that govern the behavior of a fluid in presence of gravity: the equation of motion, the equation of continuity, and Poisson's equation that relates the gravitational potential with the density distribution of matter. In this version, the exchange of energy between the thermal bath (the internal energy of the gas/fluid) and the oscillations (the kinetic energy of the macroscopic fluid motions) is neglected. This is the *adiabatic approximation* which only allows a description of the mechanical behavior of the oscillations and does not address the question of the stability of the modes (which involves thermal properties and the question of energy exchange). However, it turns out that nonadiabatic effects generally only marginally influence the value of the oscillation frequency of a pulsation mode in a stellar model, so the adiabatic version can be used with confidence for computing frequencies (periods) to sufficient accuracy to be of use in asteroseismological exercises.

The next step is to consider only small perturbations in order to be able to linearize the basic hydrodynamic equations. The unperturbed equilibrium configuration is usually that of a purely spherical stellar model. In keeping with the fundamental properties of a normal vibration mode, all perturbed quantities of interest are assumed to oscillate in phase and go through their equilibrium positions at the same time. Hence, the dependent variables that appear in the linearized equations are assumed to have a temporal dependence given by the standard oscillatory term in linear physics, i.e., $e^{i\sigma t}$, where σ is the frequency and t is the time. The technique of separation of variables is then used to characterize the spatial behavior of a mode in terms of a radial part and an angular part. For unperturbed spherical models, the angular behavior of a mode comes out, not unexpectedly, to be given by a spherical harmonic function $Y_l^m(\theta, \phi)$. One ends up with a system of 4 linear differential equations with real variables (depending now only on the radial coordinate) which, because of boundary conditions to be respected at the center and at the surface of the star model, permits only certain solutions (the modes) corresponding to specific values of the oscillation frequency σ (the eigenvalues).

A stellar pulsation mode is defined in terms of 3 discrete numbers, k, l, and m, the first one giving the number of nodes in the radial direction of the eigenfunction, and the others (l and m) being the indices of the spherical harmonic function that specifies the angular geometry of the mode. The index

k is termed the "radial order" and may take on all positive integer values, i.e., k = 0, 1, 2, etc. The index l is called the "degree" of the mode and gives the total number of nodal planes that divide the stellar sphere (l = 0, 1, 2,...). The number m is called the "azimuthal order" and its absolute value $|m|$ gives the number of nodal planes that divide the stellar sphere perpendicular to the equator while going through the poles. There are $2l+1$ possible values for m $(-l, -l+1, ...0, ...l-1, l)$. Non-rotating (spherical) stars have eigenfrequencies that are $(2l+1)$-fold degenerate in m. In that case, the period of a pulsation mode is trivially related to its angular frequency through the expression $P_{kl} = 2\pi/\sigma_{kl}$, independent of m.

It should be pointed out that there exist two distinct but complementary behaviors of gravito-acoustic waves in a spherical star, one fundamentally of acoustic origin (as in a homogeneous sphere), and the other related to the action of gravity. In terms of normal modes of vibration, these behaviors are respectively referred to as "pressure modes" (or p-modes) and "gravity modes" (or g-modes).[1] These different behaviors are related to two fundamental quantities that appear in the linearized pulsation equations: the so-called Brunt-Väisälä frequency N defined by,

$$N^2 \equiv g\left(\frac{1}{\Gamma_1}\frac{d\ln P}{dr} - \frac{d\ln\rho}{dr}\right), \tag{5}$$

and the Lamb frequency L_l defined by,

$$L_l^2 \equiv \frac{l(l+1)c^2}{r^2} \qquad \text{with} \qquad c^2 = \frac{\Gamma_1 P}{\rho} \quad , \tag{6}$$

where c is the local adiabatic sound speed and the other symbols have their standard meaning.

Consider in this context an element of fluid in equilibrium with its environment at some arbitrary depth in a star. If a perturbation is applied to this element such that it is compressed without changing position in the star, a restoring force proportional to the contrast in density (or, equivalently, to the pressure gradient) between the perturbed element and its environment will establish itself. Freed of the initial constraint, the element will react to the restoring force by oscillating in volume (density, pressure) about its equilibrium configuration. These oscillations will occur at a characteristic frequency, the Lamb frequency, which is intimately related to the local speed of sound at the equilibrium point in the star. These oscillations are then essentially acoustic in nature, and one speaks of acoustic waves or, equivalently because the restoring force is due to a pressure gradient, pressure waves. In normal situations (e.g., in stable stars), the oscillations are ultimately damped.

Consider again an element of fluid in equilibrium with its environment at some arbitrary depth in a star. This time, the perturbation consists in

[1] The gravity waves should not be confused with the gravitational waves of general relativity.

displacing the fluid element in the vertical direction, say above its equilibrium position. The element is then heavier than it should be (its density is higher than that of its new surroundings), and, freed of its initial constraint, will return toward its equilibrium position, and will oscillate up and down about it. Normally, the oscillations generated by the initial perturbation are damped over a characteristic timescale that depends on the local viscosity. These oscillations will occur at a characteristic frequency which depends on the local physical conditions at the point of equilibrium, the Brunt-Väisälä frequency. In that case, it is buoyancy that provides the restoring force and since buoyancy is directly related to the magnitude of the local gravitational acceleration, one speaks of gravity waves.

It should be clear that one cannot separate completely the effects of pressure from those of gravity. For instance, in the last example, the contrast in density (pressure) betwen the displaced element and its surroundings should also play a role. Hence, even though it is customary to divide the gravito-acoustic waves in two separate branches (one speaks of pressure modes and of gravity modes in stellar pulsation theory), the eigenfrequencies of the normal pulsation modes of a star depend at the same time on *both* the variation of the Lamb frequency with depth *and* on that of the Brunt-Väisälä frequency.

It is possible to derive a useful dispersion relation for gravito-acoustic waves by making two simplifying assumptions. The first one is the so-called Cowling approximation which consists in neglecting the perturbation of the gravitational potential. In that approximation, the adiabatic pulsation equations reduce to a system of 2 linear differential equations. Although the Cowling approximation is not very good for modes with low values of k and l and, more generally, for p-modes (it is not used in detailed numerical calculations), it is sufficient in the context of the present discussion.

The second approximation, termed the local approximation, focusses on an arbitrary shell in a stellar model in which most of the quantities appearing in the two remaining pulsation equations (speed of sound, Lamb frequency, Brunt-Väisälä frequency, local gravitational acceleration) can be seen as not varying very much in the radial direction over the shell region which, at the same time, covers a large number of radial wavelengths. This is possible only for modes with large values of the radial order k. If the radial variations are completely neglected, then one finds that the eigenfunctions have a behavior of the type $\exp(ik_r r)$, where k_r is a radial wave number that obeys the following dispersion relation,

$$k_r^2 \;=\; \frac{1}{c^2\sigma^2}\left(\sigma^2 - L_l^2\right)\left(\sigma^2 - N^2\right). \tag{7}$$

This indicates that the oscillations propagate radially (oscillatory behavior) if k_r is a real quantity or are evanescent (exponential behavior) if k_r is an imaginary quantity.

According to the dispersion relation, there exist two propagation zones in a stellar model corresponding to two distinct types of pulsation modes.

Specifically, k_r^2 is positive (and k_r is thus real) when $\sigma^2 > L_l^2,\ N^2$. This corresponds to the p-modes. Likewise, k_r^2 is again positive when $\sigma^2 < L_l^2,\ N^2$, and this occurs for the g-modes. In the regions of the star where $L_l^2 < \sigma^2 < N^2$ or $N^2 < \sigma^2 < L_l^2$, k_r^2 is negative (k_r is imaginary), and the gravito-acoustic waves are evanescent.

It is possible to obtain further qualitative information as to the behaviors of the eigenfrequencies (periods) of both p-modes and g-modes by considering two limiting cases. Specifically, in the limit where $\sigma^2 \gg L_l^2, N^2$, the above dispersion relation leads to,

$$\sigma^2 = \sigma_p^2 \simeq c^2 k_r^2 \quad . \tag{8}$$

This is the limit where essentially pure acoustic or pressure modes are found since only the speed of sound is involved in the right hand side term of equation (8). One can see that the frequency (period) of a p-mode increases (decreases) when k_r (i.e, the number of nodes in the radial direction) increases.

In the opposite limit where $\sigma^2 \ll L_l^2, N^2$, equation (7) reduces to,

$$\sigma^2 = \sigma_g^2 \simeq \frac{l(l+1)N^2}{k_r^2 r^2} \quad . \tag{9}$$

This is the limit of pure gravity modes since only the Brunt-Väisälä frequency (and no acoustic term) is involved in the expression. One can infer that the frequency (period) of a g-mode decreases (increases) when the radial order increases. In addition, the frequency (period) of a g-mode of given radial order increases (decreases) when the degree index l increases. Furthermore, g-modes with a degree index $l = 0$ – these would be radial modes – do not exist as they have a frequency of zero.

In brief, gravito-acoustic modes behave as almost pure pressure modes at very high frequencies, while they behave as almost pure gravity modes at very low frequencies. In both cases, these limits correspond to very large values of the radial order, i.e., $k \gg 1$, sometimes referred to as the "asymptotic limit". As indicated above, it is important to realize that for gravito-acoustic modes of low radial order (such as those generally observed in white dwarf stars for instance), the eigenfrequencies depend at the same time on *both* acoustic and gravity effects. Despite this, the usual nomenclature in stellar pulsation theory is to keep the terms p-modes and g-modes for all modes with radial order $k \geq 1$.

Figure 3 summarizes these considerations on the basis of an exact calculation of the low-order, low-degree period spectrum of a typical model of a ZZ Ceti pulsator. This model is characterized by a total mass $M = 0.6\,M_\odot$ and an effective temperature $T_{\rm eff} = 11{,}800$ K. It has a pure carbon core surrounded by a helium mantle containing 10^{-3} of the total mass of the star, itself surrounded by a hydrogen outer layer containing 10^{-6} of the total mass of the star. The chemical profile in the compositional transition layers has been computed under the assumption of diffusive equilibrium. The model-defining parameters

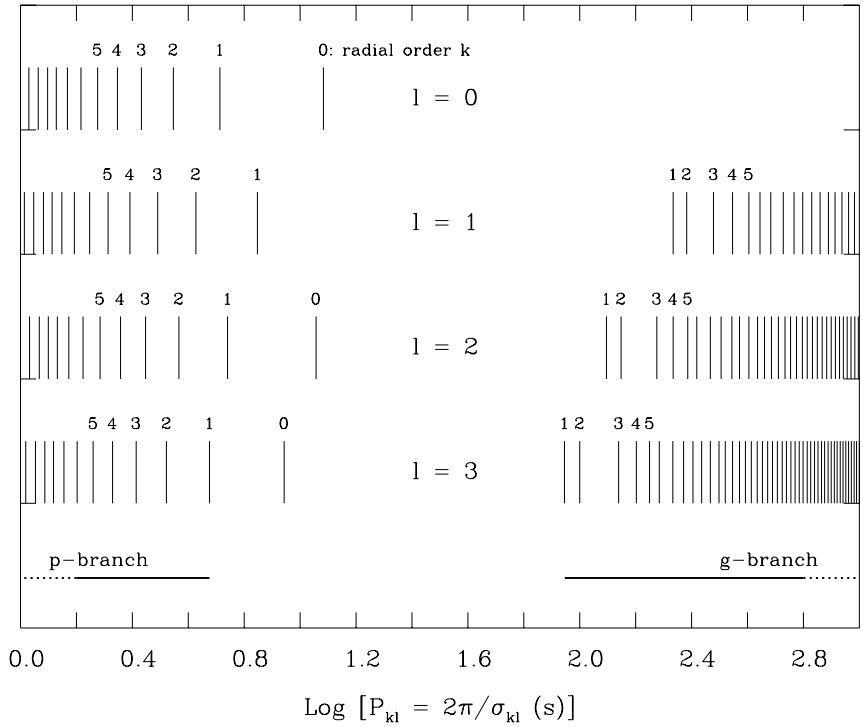

Fig. 3. Low-order and low-degree period spectrum for a representative model of a ZZ Ceti star. Results are shown for values of the degree index $l = 0$, 1, 2, and 3. The values of the radial order k are also indicated up to $k = 5$. The two families of gravito-acoustic modes, the p-modes and the g-modes, are clearly illustrated. Sometimes, depending on the convention adopted, the radial indices of g-modes are assigned negative values, so that, on a frequency scale, the values of k increase with increasing frequency over the full spectrum.

are fully representative of a ZZ Ceti star. This equilibrium structure will be used again below as a reference model.

We computed all pulsation modes with values of $l = 0$, 1, 2, and 3 in the period window 1−1000 s for our reference model. Figure 3 neatly illustrates the p-mode and g-mode branches of the gravito-acoustic period spectrum, as well as the so-called "fundamental mode" for modes with $l \geq 2$. The fundamental mode has no node in the radial direction ($k = 0$) and falls between the p- and g-branch. In white dwarfs, that mode is more akin to a p-mode than a g-mode, although, once again, it does depend on both acoustic and gravity effects. It is noteworthy that an isolated star cannot have a fundamental mode if the degree value is $l = 1$ since this would imply a motion of the center of mass during a pulsation cycle, an impossibility for a star subject to no external forces. Also, as indicated earlier, g-modes with $l = 0$ do not exist. Modes

with $l = 0$ are known as radial modes because all motions are restricted to the radial direction as there is no angular dependence ($Y_0^0(\theta, \phi) = \text{constant}$). They are simply a particular case of nonradial p-modes. Their eigenperiod spectrum does contain a fundamental mode.

It should be pointed out that a stellar atmosphere loses its capacity to reflect back toward the interior outgoing gravito-acoustic waves in the limit of very high radial order k. Indeed, in this limit, pulsation eigenmodes are strongly damped by outwardly propagating waves in the atmosphere and are not expected to belong to the gravito-acoustic cavity mentioned above. In other words, high radial order modes "leak through" the atmosphere and their energy is lost to the outside. A method for estimating these cutoff – or critical – periods in a white dwarf context has been developed by [23]. Applying this approach to the representative ZZ Ceti star model used in Figure 3, we find that p-modes with periods less than $\sim$0.1 s and g-modes with periods larger than $\sim 6000/\sqrt{l(l+1)}$ s are not expected to be of interest in that model.

4 Properties of Pulsation Modes in White Dwarfs

In the adiabatic approximation, there are four distinct eigenfunctions that come out of the numerical eigenvalue problem and which specify a given pulsation mode. It is possible to express two of those[2] directly in terms of $\xi_r(r)$ and $\xi_h(r)$, the radial and horizontal component of the Lagrangian displacement vector, respectively. The latter is given by,

$$\boldsymbol{\xi} = \left[\xi_r(r), \xi_h(r)\frac{\partial}{\partial\theta}, \xi_h(r)\frac{1}{\sin\theta}\frac{\partial}{\partial\phi}\right] Y_l^m(\theta,\phi)e^{i\sigma t}, \tag{10}$$

and has an obvious physical interpretation. In the following, we use the two distinct (radial) eigenfunctions, $\xi_r(r)$ and $\xi_h(r)$, to illustrate some interesting properties of pulsation modes in white dwarfs. Note that, for a given mode, both $\xi_r(r)$ and $\xi_h(r)$ have, of course, the same number of nodes in the radial direction (that is the radial order k of the mode), but those nodes do not overlap in space. For g-modes, the nodes of the ξ_r eigenfunction are systematically higher in the star than the corresponding nodes of the ξ_h eigenfunction. The opposite is true for p-modes.

4.1 Propagation diagram

Figure 4 is known as a "propagation diagram" and illustrates the behavior of the modes in relation to the profiles of the Brunt-Väisälä frequency and of the Lamb frequency as functions of depth. The plot refers to our representative

[2] In practice, at the numerical level, the actual eigenfunctions are conveniently expressed in terms of dimensionless quantities such as the well-renowned "Dziembowski variables" ([16]).

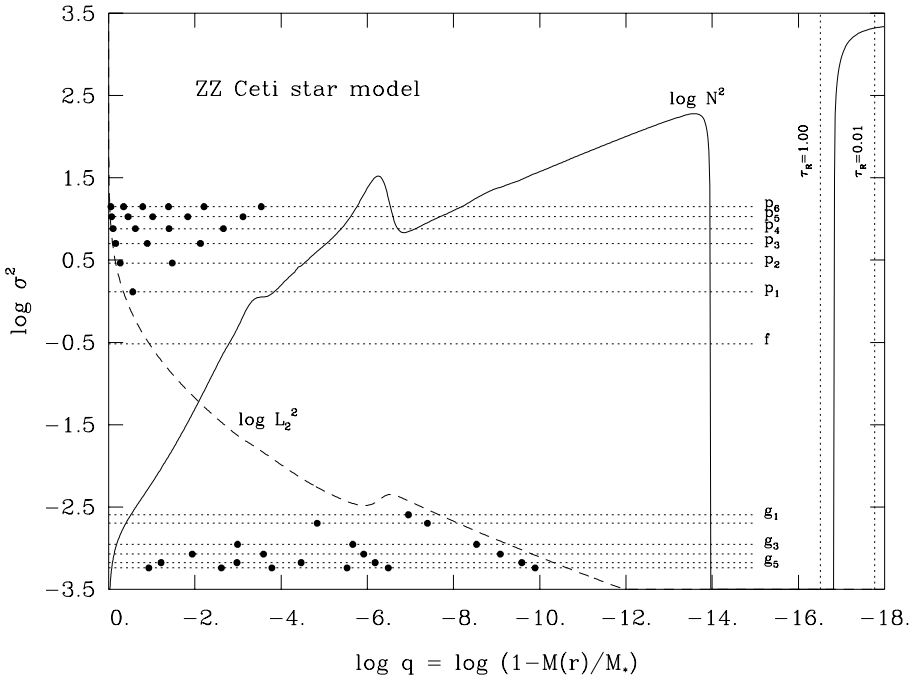

Fig. 4. Propagation diagram for quadrupole ($l = 2$) modes computed using a representative model of a ZZ Ceti pulsator. The solid curve shows the profile of the logarithm of the square of the Brunt-Väisälä frequency as a function of fractional mass depth. The value of $\log q = 0$ corresponds to the center of the stellar model. The locations of two atmospheric layers, those with $\tau_R = 10^{-2}$ and $\tau_R = 1$, are also indicated by the vertical dotted lines on that scale. Likewise, the dashed curve gives the logarithmic profile of the square of the Lamb frequency for modes with $l = 2$. The labelled horizontal dotted lines show the low-order frequency spectrum, again on a scale involving the logarithm of the square of the frequency. The dots give the locations of the nodes of the (radial) eigenfunction $\xi_r(r)$ for the different modes illustrated.

ZZ Ceti star model and features an abscissa defined by the logarithm of the fractional mass depth, a scale chosen to emphasize the outer layers where most of the "action" goes on in terms of modal behavior in white dwarfs. This scale is used repeatedly below in other figures. The solid curve shows the distribution of the logarithm of the square of the Brunt-Väisälä frequency. The well in the profile is due to the presence of a superficial convection zone caused by H partial ionization in the model. In addition, there are two bumps in the distribution of the Brunt-Väisälä frequency, one centered around $\log q \simeq -6$ and associated with the H/He compositional transition zone, and the other centered around $\log q \simeq -3$ and associated with the He/C transition zone. The former feature is stronger than the latter because there is a larger

contrast in mean molecular weight between H and He than between He and C.

The dashed curve in Figure 4 shows the profile of the logarithm of the square of the Lamb frequency for quadrupole ($l = 2$) modes, the ones chosen for this illustrative example. Bumps due again to the presence of compositional transition zones are present, but the one associated with the He/C transition region is quite weak and is hardly visible in the plot. These compositional features are significant as they "pinch" the eigenfunctions and produce mode trapping and mode confinement, ultimately leading to a nonuniform period distribution. The effect is particularly important in g-modes as can be seen in the low-order modes of the kind illustrated in Figure 3 above.

The horizontal dotted lines give the values of the logarithm of the square of the eigenfrequencies for quadrupole modes in a range covering from the $k = 6$ g-mode (termed g_6) at the low-frequency end to the $k = 6$ p-mode (termed p_6) at the high-frequency end of the retained interval. Note, in passing, the nonuniform distribution of eigenfrequencies that is particularly evident for the low-order g-modes considered here, a characteristic that was mentioned just above in the previous paragraph. The dots in the figure give the locations of the nodes in the radial direction for each of the modes illustrated. Hence, the f-mode shows no node, consistent with its radial order $k = 0$. The locations of the nodes indicate where, in a stellar model, a given pulsation mode has an oscillatory behavior in the radial direction, a region where the mode is said to propagate. Figure 4 then clearly reveals that p-modes propagate when $\sigma^2 > L_l^2, N^2$, while g-modes do when $\sigma^2 < L_l^2, N^2$. This result, coming from detailed numerical computations, is entirely consistent with the considerations presented in the previous section. In addition, Figure 4 shows that low-order p-modes in white dwarfs propagate in much deeper layers than low-order g-modes, which instead propagate in the outermost layers. Quite interestingly, this is the exact opposite of the behavior encountered in main sequence stars and in all nondegenerate stars in general.

We note, in this context, that the search for g-modes in the Sun is considered of fundamental interest in helioseismology, as a successful detection would allow the extension of asteroseismological probing of the solar interior to much deeper regions than is currently possible on the basis of the observed p-modes. In white dwarfs, only low- to medium-order g-modes have been observed so far, and it is the low-order p-modes that would allow to probe the core best. Although the presence of excited p-modes is expected from nonadiabatic pulsation theory, such modes have yet to be found in white dwarfs. The latest (unsuccessful) attempt to detect p-modes in white dwarfs using the VLT has been reported by [39].

4.2 Angular modal dependence

In a nonradially pulsating star in general, the luminosity variations are due to superficial temperature waves, changes of volume, and changes of shape, all

of which can be modeled in terms of temperature, radius, and surface gravity perturbations. In pulsating white dwarfs, it was first shown by [36] that the luminosity variations are completely dominated by temperature perturbations, a result that has been formally confirmed by [34], although the latter authors pointed out that this is not necessarily true in the cores of absorption lines. Hence, to a good approximation, the luminosity variations of a pulsating white dwarf may be visualized solely in terms of temperature waves across a disk that otherwise does not change in shape or surface area.

Figure 5 illustrates typical angular geometries for nonradial pulsation modes expected in white dwarfs, given that the modes for which the degree index has been identified so far have values of $l = 1$ or $l = 2$. One recognizes, of course, the geometries of spherical harmonic functions. Each column refers to a mode with fixed angular indices l and m, and shows the instantaneous temperature distribution on the visible disk over half a pulsation cycle covered by five distinct phases. For each of the five different modes depicted (the five columns), it is assumed that the stellar sphere is inclined such that the angle between the line-of-sight and the symmetry axis of the pulsation mode is equal to 1 radian (to be regarded as a representative value).

The first two columns refer to dipole ($l = 1$) modes, i.e., to a geometry in which there is one nodal plane that divides the stellar sphere into two equal hemispheres. The case $m = 0$ (first column) corresponds to a nodal plane that is the same as the equatorial plane (i.e., the cut is perpendicular to the symmetry axis), while the case $|m| = 1$ (second column) corresponds to a nodal plane that is akin to a great meridian plane (i.e., the cut is along the symmetry axis). It should be understood that, at any given time, all eigenfunctions of interest have zero amplitude on an angular nodal plane, from the center to the surface of the model.

The last three columns refer to quadrupole ($l = 2$) modes, i.e., they involve two nodal planes. The case $m = 0$ (third column) corresponds to two nodal planes parallel to the equatorial plane, the case $|m| = 1$ (fourth column) to one nodal plane fused into the equatorial plane and one nodal plane along the symmetry axis, and the case $|m| = 2$ (fifth column) to two nodal planes going through the pulsation axis and perpendicular to each other. It is interesting to point out that modes with $m = 0$ have nodal planes that do not change with time, whereas modes with $|m| \neq 0$ have $|m|$ planes that "rotate"about the symmetry axis. From that point of view, the angular component of a $m = 0$ mode may be considered as a standing wave, while that of a $|m| \neq 0$ mode may be considered as a running wave. Note that the two modes with the same value of $|m|$ but with different signs have similar temperature distributions (or other eigenfunctions of interest) that "rotate" at the same absolute speed about the symmetry axis, but one clockwise and the other counterclockwise. It should be noted that the "rotation speed" is directly related to the eigenfrequency σ.

Figure 5 shows further that for standing angular waves ($m = 0$ modes), the instantaneous temperature distribution becomes uniform across the visible

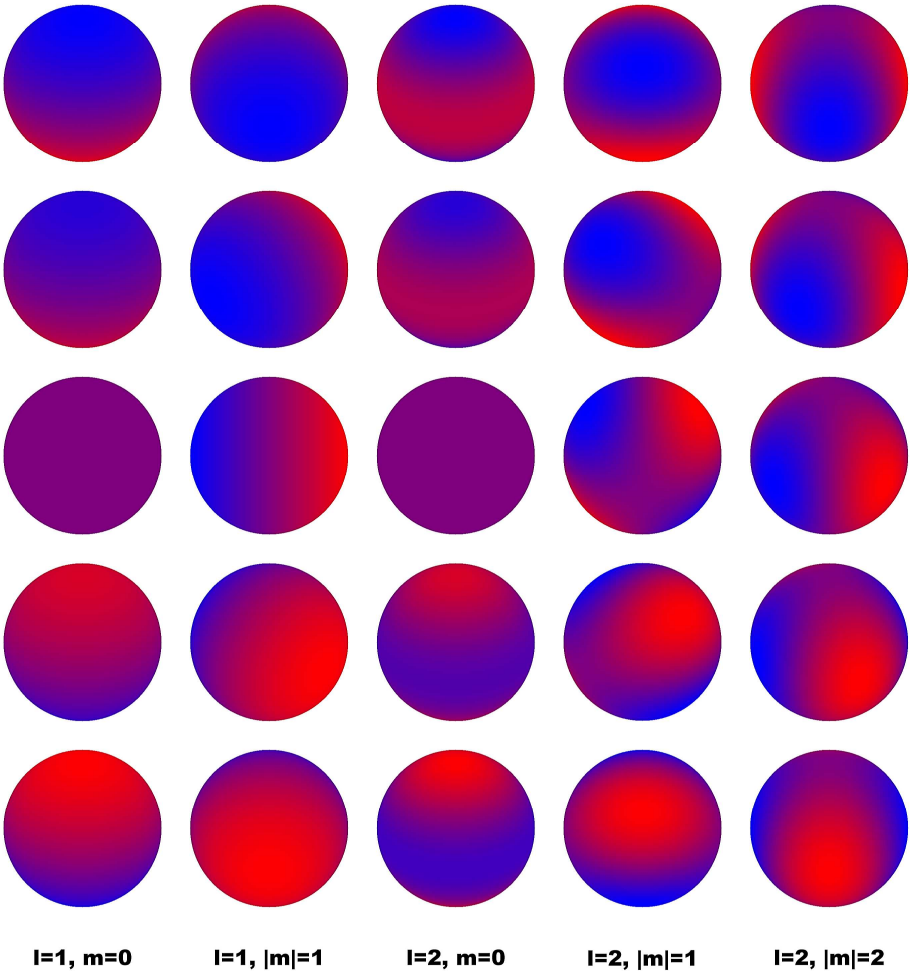

Fig. 5. Instantaneous temperature distributions on the visible disk of a white dwarf model for different modal angular geometries. Each column refers to a given pair (l,m), and covers half a pulsation cycle in five phases. The pulsation frequency is arbitrary and remains undefined in this plot. In each case, the angle of inclination between the line-of-sight and the axis of symmetry of the pulsation has been fixed to 1 radian. The color code is such that the deepest blue may correspond to the highest local temperature (above the average one), the deepest red may correspond to the lowest local temperature (below the average), and purple corresponds to the average unperturbed temperature.

disk twice during a pulsation cycle. This is well illustrated in the first and third column for the phase corresponding to 1/4 of a full cycle. In contrast, running angular waves ($|m| \neq 0$) never show a phase when the temperature distribution is uniform across the visible disk. Finally, for completeness, it should be remembered that pulsation modes with a value of the azimuthal order $m = 0$ are sometimes referred to as "zonal modes", while those with $l = |m|$ are called "sectorial modes".

4.3 Radial modal dependence

Figure 6 illustrates the typical radial dependence of the ξ_r and ξ_h eigenfunctions corresponding, respectively, to the radial and horizontal component of the displacement vector in a pulsating white dwarf. We again refer to our representative ZZ Ceti star model, and we consider the lowest order quadrupole modes from g_5 to p_5, including the f-mode.

The upper panel of the figure depicts the profile of ξ_r as a function of depth for the f-mode, three low-order p-modes (p_1, p_3, and p_5), and the three corresponding low-order g-modes (g_1, g_3, and g_5). The modes with radial order $k = 2$ and $k = 4$ were not plotted in order to not clutter the diagram too much. In keeping with our remark above in Section 2 related to the linear approach, the amplitudes of the eigenfunctions in the linear theory of stellar pulsations have to be arbitrarily normalized at some convenient value and location. Here, the amplitude of the ξ_r eigenfunction has been normalized to the value of one at the surface of the model for each mode considered, i.e., $\xi_r(r = R) = 1$. Hence, a comparison of the ξ_r profiles for various modes becomes meaningful if one understands that the amplitudes of all the modes are normalized to be the same at the surface of the star.

One can see that the amplitudes of the low-order p-modes are generally much larger than those of the low-order g-modes in the deeper layers. The latter exhibit nodes much higher in the star than the former (these nodes are, of course, the same as those shown in Figure 4 above). It is interesting to observe that the f-mode keeps the largest amplitude over the full stellar model. Also, the g_3 mode behaves differently from the g_1 and g_5 modes in that its amplitude in the stellar core remains comparatively large, whereas the two other modes show very small amplitude values at these depths. This is because the g_3 mode is partially confined *below* the H/He transition layer due to a resonance condition: the second node in ξ_r (counting from the surface inward) falls just below the H/He compositional transition zone, while, at the same time, the first node in ξ_h falls just above. The corollary condition for trapping of a g-mode *above* a compositional transition zone is that the n^{th} node of the ξ_r eigenfunction falls just above the transition region, while the n^{th} node of the ξ_h eigenfunction falls just below. This notion of mode confinement and mode trapping for g-modes in white dwarfs caused by the onion-like compositional stratification has thoroughly been discussed by [4], including these conditions

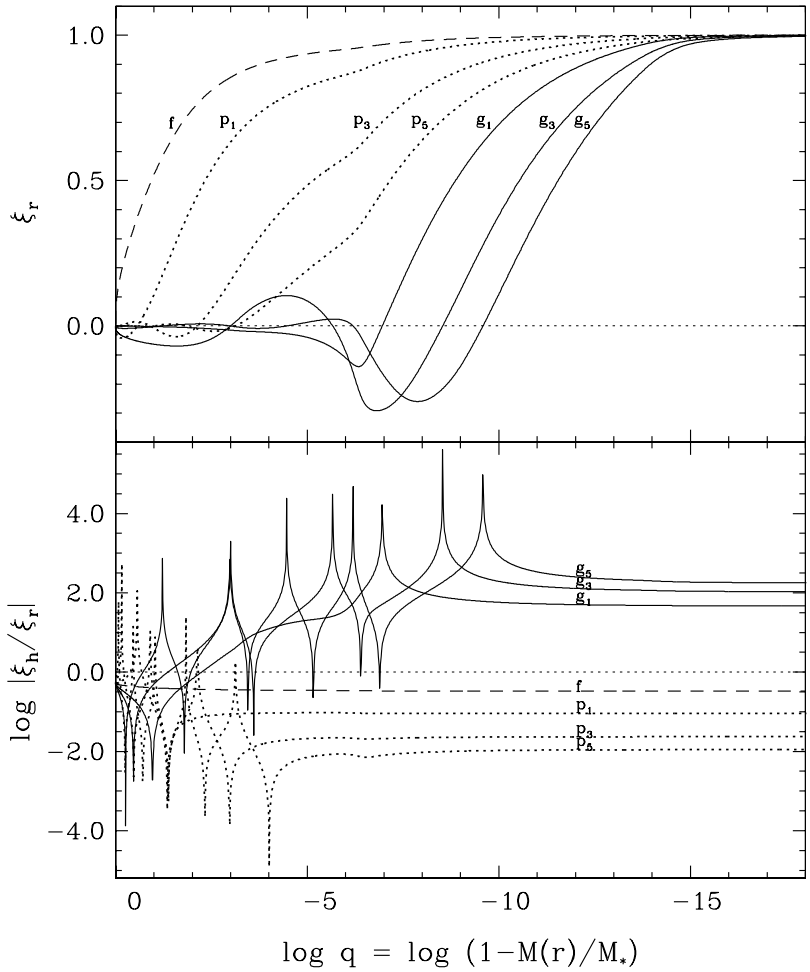

Fig. 6. *Upper panel:* Profile of the radial eigenfunction ξ_r as a function of depth for the lowest order quadrupole modes in our reference ZZ Ceti star model. *Lower panel:* Absolute ratio of the horizontal to the radial component of the displacement vector for the same modes.

of resonance. The reader is referred to that paper for more details. We briefly revisit the concept of mode confinement/trapping below.

The lower panel of Figure 6 shows the absolute ratio of the horizontal to radial components of the displacement vector as a function of depth for the same modes. This is a particularly interesting plot as the results are independent of the actual normalization adopted. That is, whatever the actual amplitude of a mode, linear theory predicts a *given* amplitude ratio between $|\xi_h|$ and $|\xi_r|$ as shown in the figure. The maxima in the curves correspond to

the nodes in the ξ_r eigenfunction, while the minima correspond to the nodes in the ξ_h eigenfunction. As indicated above, the number of nodes for a given mode is the same for the radial and horizontal displacement eigenfunctions, but they do not fall at the same locations in the star.

It is quite instructive to focus on the amplitude ratio at the surface of the model. Thus, in the observable atmospheric layers of a pulsating white dwarf, matter is displaced much more horizontally than vertically during the pulsation cycle of a g-mode. Indeed, according to the lower panel of the figure, the ratio of the horizontal to radial components of the displacement vector already exceeds 100 for a $k = 3$ mode, and it increases rapidly with increasing radial order. Conversely, the ratio of the *radial to horizontal* displacement increases rapidly with increasing radial order for p-modes, reaching nearly 100 for the p_5 mode illustrated in Figure 6. The contrast between horizontal and radial displacements is even larger for $l = 1$ modes, being some three times larger for the $k = 3$ g-mode than the g_3 quadrupole mode shown in the figure. It is therefore certain that the g-modes observed in pulsating white dwarfs correspond to material motions that are essentially horizontal in the superficial layers. The very large surface gravity characteristic of white dwarfs ($\log g \sim 8$) is at the origin of this phenomenon.

4.4 Kinetic energy

An interesting global property of a pulsation mode is its kinetic energy defined by the general relation,

$$E_{\rm kin} \equiv \frac{1}{2} \int_V \rho v^2 \, dV \qquad , \tag{11}$$

where the integration is carried out over the total volume occupied by the star. If one neglects the rotation of the star and any other possible macroscopic velocity field (such as convection or meridional circulation), one can express the kinetic energy in terms of a radial integral involving the two eigenfunctions ξ_r and ξ_h,

$$E_{\rm kin} \equiv \frac{\sigma^2}{2} \int_0^R \left[\xi_r(r)^2 + l\,(l+1)\,\xi_h(r)^2 \right] \rho r^2 \, dr \qquad . \tag{12}$$

Given the arbitrary normalization of the eigenfunctions in linear theory, the kinetic energy of a mode is known only to within a multiplicative factor. In practice, this means that only relative comparisons between the kinetic energies of different modes have a physical sense. Hence, to excite a mode with the *same observable amplitude* at the surface of a star as that of a reference mode requires (more or less) energy, and that increment is given by the difference, $\Delta E_{\rm kin}$, between the kinetic energies of the two modes.

Figure 7 shows the distribution of the kinetic energy as a function of the period for the series of quadrupole modes with periods falling between

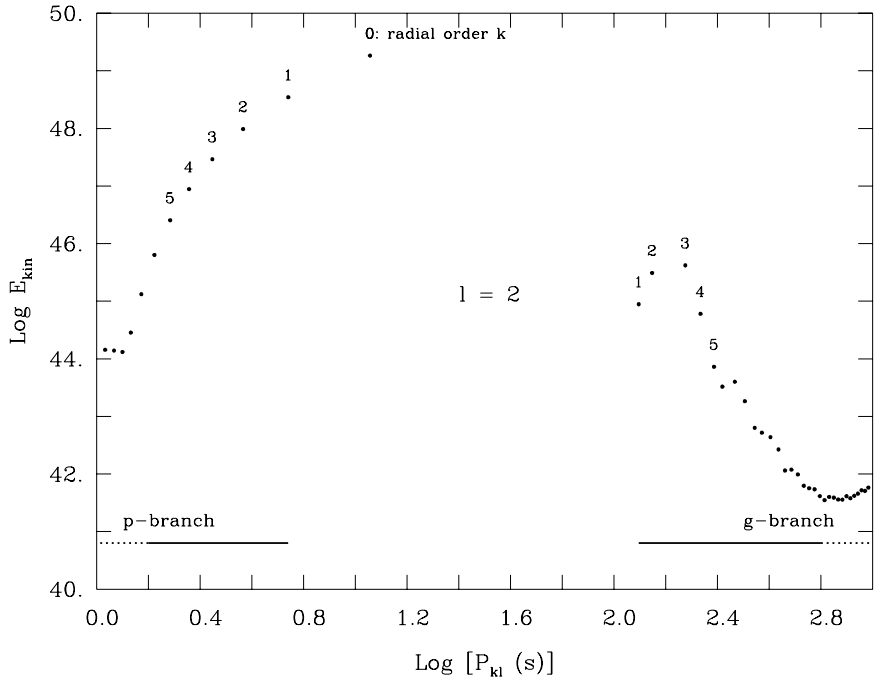

Fig. 7. Kinetic energy as a function of period for the family of quadrupole modes with periods in the range from 1 s to 1000 s as computed using our reference ZZ Ceti model.

1 s and 1000 s as computed on the basis of our representative ZZ Ceti star model. Given the behavior of its displacement eigenfunctions – as can be observed in Figure 6 – in conjunction with equation (12), it is not surprising that the f-mode comes out with the largest kinetic energy of the lot. Indeed, the amplitude of the fundamental mode (both in ξ_r and ξ_h) is basically larger than any other mode over the whole stellar model. This means that the f-mode requires the most energy to be excited to a given surface amplitude. Sometimes, such a mode is referred to as the one with the most "inertia".

The fact that the low-order p-modes have significantly larger amplitudes than their g-mode counterparts in the deeper regions of a white dwarf (see again Figure 6), combined with the large values of the density ρ at these depths compared to its envelope values, readily explains why the kinetic energies of the p-modes are much larger than those of the g-modes. This is an important characteristic of white dwarf stars. In addition, the eigenfunctions depicted in Figure 6 for both p-modes and g-modes exhibit an outward "migration" with increasing radial order in the sense that their amplitudes tend to drop to very small values in an outwardly growing region from the center. This explains

the significant drop of the kinetic energy with increasing radial order along the two branches of nonradial modes.

The case of g-modes merits further discussion as these are the modes observed in real pulsating white dwarfs. For instance, a mode like g_3 in Figure 7 shows a local maximum in kinetic energy along the g-branch. As briefly alluded to above, such a mode can be seen as partially confined below the H/He transition zone. It exhibits the larger amplitudes below that region as compared to other g-modes and, therefore, it has a larger kinetic energy. Conversely, the g_6 mode shows a local minimum in kinetic energy due to the fact that it tends to be partially trapped above the H/He transition zone, with the consequence that it has lower amplitudes below that region as compared to its immediate adjacent modes.

4.5 Weight function

It has been shown by [27] (and see also [7]) that the eigenvalues of the adiabatic pulsation equations can be estimated from a variational approach. For a purely spherical model, the square of an eigenfrequency is given by,

$$\sigma^2 = \frac{D}{A} \quad , \tag{13}$$

where D and A are two integral expressions involving the eigenfunctions of that eigenfrequency. This expression can be used, after the solution of the eigenvalue problem has been obtained, to derive a variational estimate of the eigenfrequency. While this is generally less accurate than the result provided by the eigenvalue itself, in part due to the fact that the boundary conditions used in the variational approach are not exactly the same as those used in the eigenvalue problem, the approach is often used as a measure of internal consistency. Of greater interest, however, is the fact that equation (13) involves *integral expressions* over the stellar model. While the integral A appearing in the denominator is simply proportional to the kinetic energy defined above, the *integrand* of the integral D appearing in the numerator provides a measure of the contribution of each shell in the stellar model to the overall integral. As such, the integrand of the integral D for a given pulsation mode is often referred to as the "weight function" of the mode. This concept is very useful for inferring which regions of a stellar model contribute most to the formation of a mode. The integral D may be written,

$$D = \int_0^R \left[\xi_r^2 N^2 + \frac{(P')^2}{\Gamma_1 P \rho} + \Phi' \left(\frac{P'}{\Gamma_1 P} + \xi_r \frac{N^2}{g} \right) \right] \rho r^2 \, dr \quad , \tag{14}$$

where two other adiabatic eigenfunctions explicitly appear: Φ' (the Eulerian perturbation of the gravitational potential), and P' (the Eulerian perturbation of the pressure).

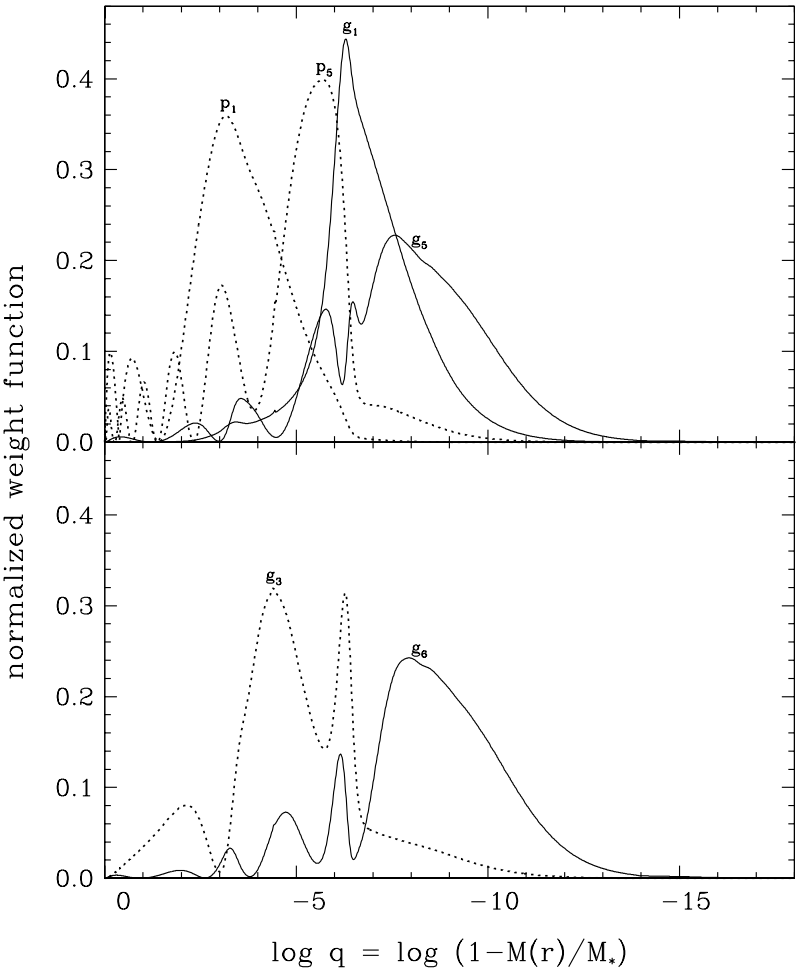

Fig. 8. *Upper panel:* Normalized weight function as a function of depth for a few low-order quadrupole modes in our reference ZZ Ceti star model. The normalization insures that the area under each curve is the same. *Lower panel:* Normalized weight function for a confined mode (g_3) and a trapped mode (g_6).

Figure 8 illustrates the weight functions for a few of the low-order quadrupole pulsation modes that have been discussed above for our representative white dwarf model. The weight function of each mode is normalized such that the area under each curve is the same. In keeping with our previous discussion, it is not surprising to observe in the upper panel that a p-mode of a given radial order has a weight function indicating a sensitivity to much deeper layers than its corresponding g-mode. Again, this indicates that p-modes depend more on

the physical conditions in the interior than g-modes do. The latter are mostly envelope modes in cool pulsating white dwarfs such as ZZ Ceti stars.

The lower panel of Figure 8 shows the weight functions of the quadrupole modes g_3 and g_6 that have been discussed above. The former is partially confined below the H/He transition zone centered on $\log q \simeq -6$, while the latter is partially trapped above that compositional transition region. Clearly, their weight functions reflect this state of affair. It should be evident that this concept of mode confinement/trapping must be seen as the result of a (relatively weak) partial wave reflection in the transition layers, allowing the confined mode to extend above the transition region, and the trapped mode to extend below that region. The modes remain global (as always), but they are more sensitive to the conditions found above or below, depending on whether or not they are trapped or confined.

It is very instructive to investigate the evolution of the weight function of a pulsation mode along the evolutionary track followed by a cooling white dwarf. In this way, one can appreciate the change of regime from the GW Vir hot phase of evolution to the cool ZZ Ceti phase (which has been emphasized through the use of our reference model in the illustrative examples presented so far). Along the cooling track (see, e.g., the curves shown in Figure 1), the overall degeneracy of a white dwarf model increases and this pushes the region of g-mode formation outwards. This implies that mode sensitivity to model parameters changes from the GW Vir phase to the V777 Her phase and the ZZ Ceti regime.

This notion of changing mode sensitivity along the white dwarf cooling track is well illustrated in the top panel of Figure 9. In order to avoid the complications caused by chemical layering, i.e., mode confinement and trapping which would cause the weight function not to behave monotonically and confuse the plot, the evolution of a *pure* C model was considered. The figure shows the weight function of the lowest-order (k =1) dipole g-mode in terms of depth, and in terms of different phases of cooling as quantified by the effective temperature. The weight function is again normalized so that the area under each curve is the same. Figure 9 clearly reveals the *outward migration* of the region of g-mode formation with cooling. This implies that the pulsation modes of a white dwarf (the g-modes as observed) progressively lose their ability to probe the deep interior (GW Vir regime) and become more sensitive to the details of the outermost layers (ZZ Ceti regime) as cooling proceeds. It is particularly obvious here that the k =1, l = 1 g-mode in the 10,117 K model does not probe the core very well.

The panel at the bottom of Figure 9 illustrates, in contrast, the fact that there is little migration of the region of mode formation for a p-mode in an evolving white dwarf. There is *some* outward migration, particularly below 30,000 K, but the effect remains mild. Hence, even at $T_{\rm eff}$ = 10,117 K, the p_1 mode still probes the deep core as it did at much higher effective temperatures. The g-modes are thus much more sensitive to the outward progression of the degeneracy boundary in an evolving white dwarf than p-modes can be. The

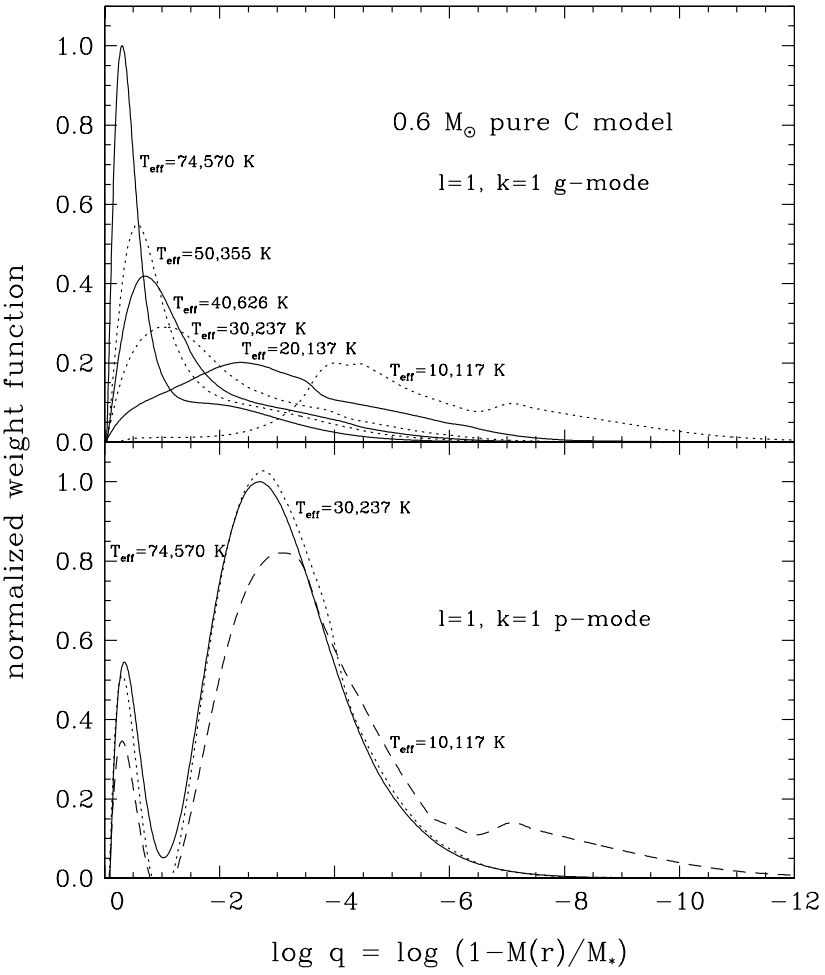

Fig. 9. *Upper panel:* Evolution of the normalized weight function for the lowest-order dipole g-mode in a series of models culled from an evolutionary sequence of pure C white dwarfs. *Lower panel:* Similar, but for the lowest-order dipole p-mode.

reason for this is to be found in the different behavior of the Brunt-Väisälä frequency compared to that of the Lamb frequency.

4.6 Rotational splitting

The variational approach put forward by [27] is again of great use for estimating the effects of slow rotation on the eigenfrequency spectrum of a pulsating star. In practice, "slow rotation" means that $\Omega \ll \sigma$, where Ω is the rotation frequency of the star. The variational method allows the treatment of slow ro-

tation as a perturbation and leads to corrections to the eigenfrequencies that are given in terms of *integral expressions* involving the unperturbed eigenfunctions, i.e., those coming out of the solution of the eigenvalue problem for purely spherically symmetric models (such as ξ_r and ξ_h encountered above).

The main effect of slow rotation is to destroy the spherical symmetry of the star and, as a consequence, the $(2l+1)$-fold degeneracy that exists for the eigenfrequencies of modes with different values of m but belonging to the same pair (k,l) in a nonrotating model is lifted. Under the assumption that the angular rotation frequency is a simple function of depth, $\Omega(r)$, the frequency of a mode, now defined by the three indices k, l, and m, is given through first-order perturbation theory by,

$$\sigma_{klm} \simeq \sigma_{kl} - m \int_0^R \Omega(r) K_{kl}(r) dr \quad , \tag{15}$$

where σ_{kl} is the frequency of the degenerate modes (k,l) in the absence of rotation, and the second term on the right side is the first-order correction to that frequency, with m taking on the values $-l, -l+1, ..., l-1, l$. The quantity $K_{kl}(r)$ appearing in the correction term is referred to as the first-order rotation kernel. It obviously plays the role of a weight function, very much similar to the weight function discussed above for the eigenfrequency, but, this time, referring to the regions contributing to the frequency splitting due to rotation. It is given by the following expression involving the unperturbed eigenfunctions,

$$K_{kl}(r) = \frac{\{\xi_r^2 + [l(l+1)-1]\xi_h^2 - 2\xi_r\xi_h\}\rho r^2}{\int_0^R \{\xi_r^2 + l(l+1)\xi_h^2\}\rho r^2 \, dr} \quad . \tag{16}$$

If the star is further assumed to rotate as a *solid body* ($\Omega \neq \Omega(r)$), equation (15) reduces to,

$$\sigma_{klm} \simeq \sigma_{kl} - m\Omega(1 - C_{kl}) \quad , \tag{17}$$

where Ω is the (uniform) angular rotation frequency, and C_{kl} is a dimensionless quantity named the first-order solid body rotation coefficient (or Ledoux coefficient). It is given by,

$$C_{kl} = \frac{\int_0^R \{2\xi_r\xi_h + \xi_h^2\}\rho r^2 \, dr}{\int_0^R \{\xi_r^2 + l(l+1)\xi_h^2\}\rho r^2 \, dr} \quad . \tag{18}$$

Given the solution of the eigenvalue problem for a mode, equation (18) allows the evaluation of the C_{kl} coefficient for that mode. Note that first-order solid body rotation leads to a set of equally-spaced frequencies with a splitting between adjacent frequency components given by,

$$\Delta\sigma = \Omega\,(1 - C_{kl}) \quad . \tag{19}$$

Figure 10 shows the values of the first-order solid body rotation coefficient for a series of quadrupole modes (the same as those illustrated in Fig. 7) covering the period interval 1−1000 s, and referring to our representative white dwarf model. As is the case for all types of stars, the values of C_{kl} for p-modes tend to become very small compared to 1 in the asymptotic limit of high radial order. In contrast, the values of C_{kl} for g-modes tend towards a nonzero value, $1/(l(l+1))$, in the same limit, as can be seen in the figure for $l = 2$. Note that the lowest-order g-modes – of most interest for pulsating white dwarfs – show significantly different values of C_{kl} from one mode to another, a good thing because this may help in constraining the radial order of a mode versus another one in presence of observed rotational splitting.

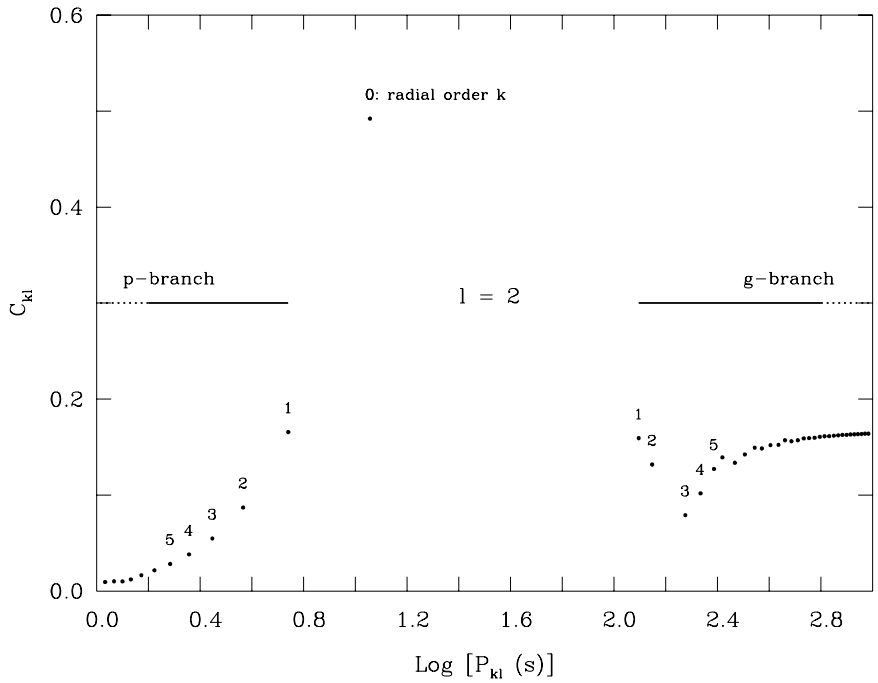

Fig. 10. First-order solid body rotation coefficient as a function of period for the family of quadrupole modes with periods in the range from 1 s to 1000 s as computed on the basis of our reference ZZ Ceti star model. The format is similar to that of Fig. 7 above, and the modes considered are the same.

Figure 11 shows examples of frequency spectra, with and without rotation, obtained from our reference white dwarf model. A relatively small value of 3 h was assumed for the rotation period of the model in order to clearly see the split components in frequency space. Note that such a value is "slow" from a dynamical point of view for a compact star such as a white dwarf. In practice,

rotational splitting has been detected and used to infer the rotation period of some 14 pulsating white dwarfs so far (see Table 4 of [17]). The inferred rotation periods vary from 5 h to 55 h, which is again quite slow.

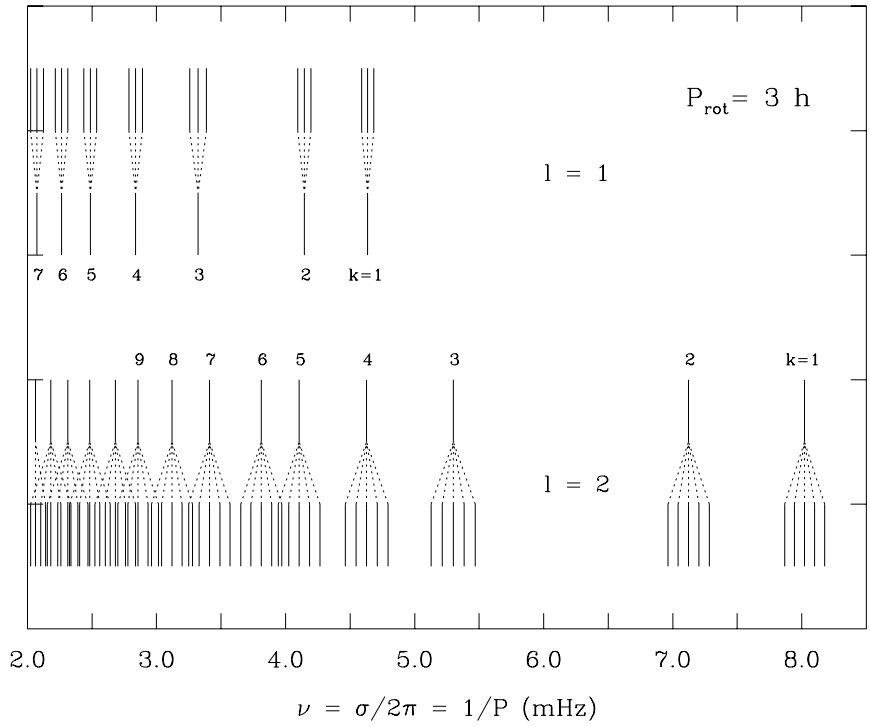

Fig. 11. Rotational splitting in our representative ZZ Ceti star model. The low-order g-mode frequency spectra for both dipole and quadrupole modes, with and without rotation turned on, are illustrated. It is assumed that the star rotates as a solid body and with a (relatively) short period of 3 h. Degenerate dipole modes split into triplets, while quadrupole modes split into quintuplets. The spacings between adjacent components within a given multiplet are the same in frequency space as shown here.

5 Period Evolution

Another observable of high potential interest for white dwarf asteroseismology is the rate of period change of a mode in a given pulsating star. If the period change is due primarily to the secular evolution of the star, and not to external causes such as, e.g., the cyclic orbital motion in a close binary or planet-harboring star, then adiabatic asteroseismology can be used to infer additional

properties or confirm/test the properties derived from using the period data in a standard asteroseismological exercise.

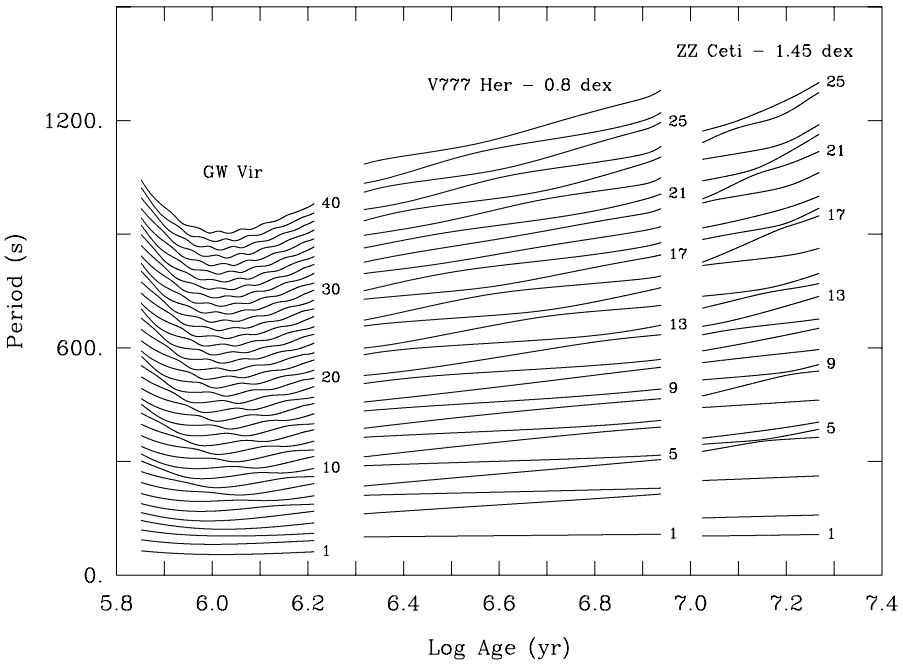

Fig. 12. Representative examples of period evolution for dipole g-modes during the GW Vir, V777 Her, and ZZ Ceti phases. Note the offset in age between these different phases of evolution. The radial order k is indicated for some of the modes depicted here.

Figure 12 is meant to illustrate how pulsation periods typically evolve for the three main categories of pulsating white dwarfs that are known: the GW Vir, V777 Her, and ZZ Ceti stars. In each case, the evolving model is specified by a total mass of 0.6 $M_{\odot}$ and a uniform core composition made of carbon and oxygen in the same proportions by mass fraction. The envelope in the GW Vir model is made of a representative PG1159 composition (X(He)=0.38, X(C)=0.40, and X(O)=0.20) and contains 10^{-2} of the total mass of the star. The envelope of the V777 Her model also has an envelope representing 10^{-2} of the total mass of the star, but it is made of pure helium. In the case of the ZZ Ceti model, there is a pure helium mantle containing a mass fraction of 10^{-2} surrounded by a pure hydrogen envelope containing 10^{-4} of the total mass. Given the different timescales involved – the evolution of a white dwarf considerably slows down with decreasing luminosity – and our desire to plot the results in the same figure, we used the logarithm of the cooling time (with

respect to some arbitrary zero point) as the abscissa and we introduced a shift of -0.80 (-1.45) dex for the V777 Her (ZZ Ceti) model.

For each type of pulsator of interest, the lower part of the dipole g-mode spectrum (starting with $k = 1$) was computed for several equilibrium configurations mapping the instability strip. In the case of the GW Vir phase, the equilibrium models considered cover the "turning of the bend" in the HR diagram (see, e.g., Fig. 1) corresponding to the final contraction phase during which the star gets hotter and more compact and the pulsation period of a mode decreases, followed by the beginning of the cooling phase during which the star gets cooler and (slightly) more compact and the pulsation period increases. The period of a g-mode in a GW Vir model goes through a minimum practically when the model reaches its maximum effective temperature in its excursion in the HR diagram. Things are simpler for the V777 Her and ZZ Ceti families which correspond to purely cooling phases and, therefore, such stars exhibit pulsation periods that increase monotonically with passing time, although not at the same rate from one mode to another as can be appreciated in Figure 12. The increase of the pulsation period of a g-mode in a cooling white dwarf is intimately related to the outwardly growing degenerate region which has the effect of lowering the value of the Brunt-Väisälä frequency.[3]

It should be noted that the phases covered in Figure 12 encompass the empirical instability strips and are meant to be primarily illustrative. For instance, the coolest model considered in the GW Vir phase is somewhat cooler at $T_{\rm eff} \simeq 77{,}000$ K than the actual observed red edge. Also, the V777 Her phase maps a range of effective temperatures from about 28,000 K to 21,000 K, while the ZZ Ceti phase covers an interval from about 13,000 K to about 10,300 K, somewhat larger than the widths of the observed instability strips. It should further be noted that the figure reveals significant wavy structures in the computed period distributions, most obvious for the GW Vir phase. These structures, sometimes referred to as "mode bumpings" and "avoided crossings", are due to the phenomenon of mode trapping/confinement at compositional transition layers in our white dwarf models. Purely radiative models with a uniform chemical composition would not show these wavy features.

In the case of the GW Vir model, in particular, the nodes of a given radial overtone first migrate inwards and then outwards as the model turns around the bend in the spectroscopic HR diagram. These nodes successively pass through the composition transition region at the interface of the C/O core and the envelope, where conditions for partial mode confinement or trapping are met. Hence, a given mode is alternatively partially trapped and partially confined as a function of time, and this produces the period variations that can be seen in Figure 12. For higher order modes, the nodes are more numerous and closer together, so there are more "waves" in their temporal period distribution as can also be observed in the figure.

[3] For a completely degenerate, zero-temperature stellar configuration, the Brunt-Väisälä frequency is strictly equal to zero.

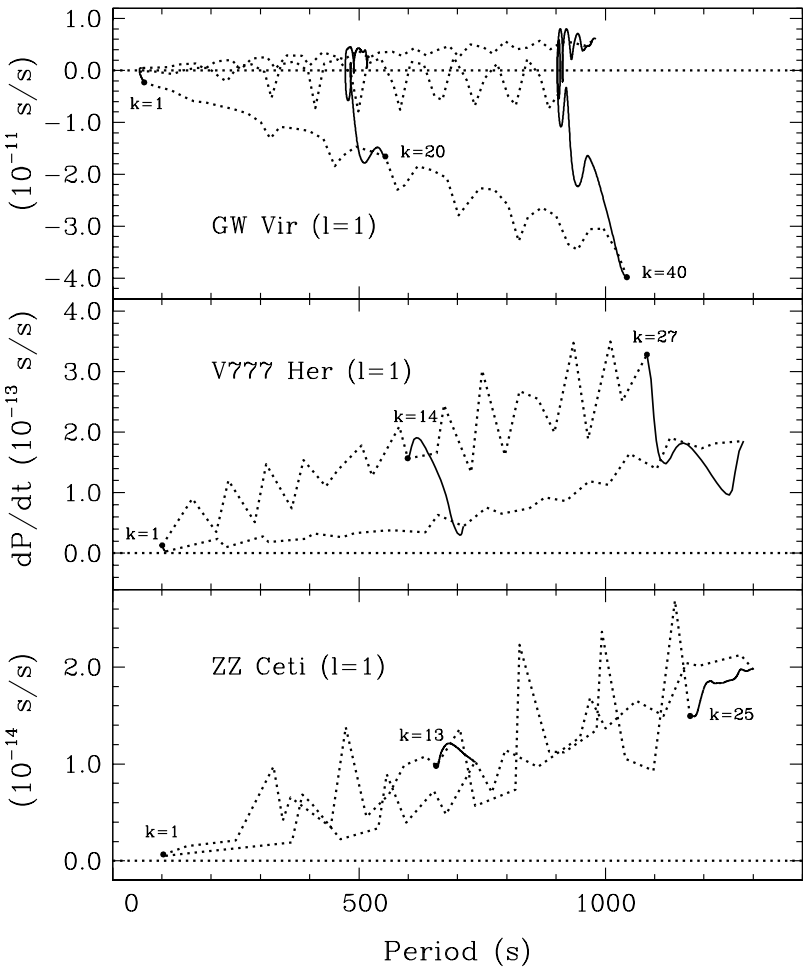

Fig. 13. *Upper panel:* Evolution of the rates of period change for three representative dipole modes ($k = 1$, $k = 20$, and $k = 40$) across the GW Vir instability strip. The evolutionary paths are shown by the solid curves and start with a dot. The dotted curves show the values of dP/dt for the 40 overtones at three distinct epochs during the evolution. *Middle panel:* Similar, but for the $k = 1$, $k = 14$, and $k = 27$ overtones across the V777 Her instability strip. Also, only the initial and final distributions for the 27 modes are shown by the dotted curves. *Lower panel:* Similar to the middle panel, but for the $k = 1$, $k = 13$, and $k = 25$ modes in the ZZ Ceti strip.

Figure 13 shows some results for values of the rates of period change computed from these evolutionary sequences. As expected from the wavy structure illustrated in the previous figure, the behavior of dP/dt as a function of time for a given mode, and as a function of radial order for a given epoch, is rather

complicated. For instance, in the upper panel of Figure 13, the evolutionary paths followed by dP/dt for dipole g-modes with $k = 1$, $k = 20$, and $k = 40$ are illustrated by the solid curves. The starting point for each path is indicated by a small dot, and this corresponds to an early epoch when the model enters the GW Vir region at low gravity and (relatively) low effective temperature, still contracting and getting hotter. The dotted curve connecting the three "starting" points shows the spectrum of dP/dt values for the first 40 dipole overtones when the model enters the strip. The quasi-periodic behavior along the spectrum is again due to mode trapping/confinement effects. The spectrum is equivalent to measuring the slope for each of the 40 modes on the left side of the 40 curves shown in Figure 12 and referring to the GW Vir regime. In this early phase, all slopes are negative and the dP/dt values for a contracting model of a pre-white dwarf are all negative.

In contrast, by the time the model exits the GW Vir domain as a high-gravity cooling white dwarf with $T_{\rm eff} \simeq 80{,}000$ K, all values of dP/dt are positive (top dotted curve in the upper panel of the figure). In between, there exist epochs when, in a given model, one can find *both* modes with positive values of the rate of period change *and* modes with negative values, depending on their radial order. This is illustrated by the middle dotted curve in that same panel, which corresponds to an evolutionary phase near the turning of the bend in the HR diagram. This particular circumstance, if observed, may be of high value for pinning down the precise evolutionary status of a GW Vir pulsator.

The evolutionary paths shown in Figure 13 are complicated in that they again reflect the effects of mode trapping/confinement. For instance, the path for the $k = 40$ mode crosses the zero value several times, meaning that the rate of period change for that particular mode is initially negative, then changes sign a few times around the turning of the bend, and finally takes on a positive value by the time the star leaves the GW Vir region. This path is equivalent to measuring the slope along the GW Vir $k = 40$ curve in Figure 12.

For their part, dP/dt values for g-modes due to secular evolution are *always* positive for V777 Her and ZZ Ceti pulsators as can be seen in both Figures 12 and 13. This is due to the fact that white dwarfs in these evolutionary phases are purely cooling bodies and that the overall decrease of the Brunt-Väisälä frequency in their internal regions due to the growing degeneracy pushes the periods of g-modes to higher values. Of notable interest, Figure 13 also reveals that the values of dP/dt for modes of comparable radial order decrease substantially along the white dwarf cooling sequence. For instance, the typical order of magnitude for the rate of period change for a GW Vir pulsator is $dP/dt \sim 10^{-11}$ s/s, for a V777 Her star it is $dP/dt \sim 10^{-13}$ s/s, and for a ZZ Ceti pulsator it drops to the low value of $dP/dt \sim 10^{-14}$ s/s. These numbers simply reflect the very different evolutionary timescales that characterize these three phases. The numbers show that it is *much* more difficult to measure the rate of period change of a mode in a ZZ Ceti star than it is in a GW Vir pulsator.

It should be realized that the measurement of dP/dt for a mode in a pulsating white dwarf, assuming that such measurement is available and credible, is not easy to interpret without having first derived a reliable seismic model for the pulsator under scrutiny. Such a model, obtained from the analysis of the period data (and additional input such as multicolor photometry as may be the case), provides estimates of the structural parameters of the pulsator and a mode identification. These are *essential* ingredients required for interpreting the measurement of the rate of period change. And indeed, it can be shown that a given value of dP/dt may be shared by modes with different radial order or degree index, or by models with different masses, envelope layerings, core compositions, and effective temperatures. Hence, it is absolutely necessary to know these parameters to a good level of accuracy before attempting to exploit the dP/dt data.

Figure 14 summarizes the results of numerical experiments featuring representative modes of interest (dipole g-modes with $k = 1, 8$, and 15) for models of ZZ Ceti stars. It shows how the values of dP/dt for these modes change as the models cool through the ZZ Ceti instability strip. In the upper panel, two similar models are used: they both have a total mass of 0.6 $M_\odot$, a uniform core composition made of carbon and oxygen in the same proportions by mass fraction, and a pure helium mantle containing a mass fraction of 10^{-2}, but they differ in that one (dashed curves) has a pure H outermost envelope containing a mass fraction of 10^{-4} (let us call it the "reference model" in this Section), while the other (solid curves) has a much thinner hydrogen layer of mass fraction 10^{-10}. In the same spirit, the middle panel of the figure refers to the reference evolutionary model (dashed curves) and a similar one (solid curves) differing only in its total mass, now equal to 0.9 $M_\odot$. Likewise, the lower panel refers to additional models similar to the reference model (dashed curves), but one having a pure C core composition (solid curves), and the other a pure O core composition (dotted curves).

There are some differences between the values of dP/dt for the lowest-order ($k = 1$) mode considered in Figure 14 depending on the model parameters, but these differences remain small on the scales used here, and they are much smaller than those found for the higher order modes. Generally speaking, the rates of period change are highly dependent on modal and model parameters. It should therefore be clear from this that the interpretation of a dP/dt measurement must rest on the availability of a reliable seismic model.

6 The Nonadiabatic Approach

6.1 Basic considerations

In its full version, the linear theory of nonradial stellar pulsations takes into account the energy exchanges between the environment and the macroscopic fluid motions during a pulsation cycle. Two more hydrodynamic equations, the

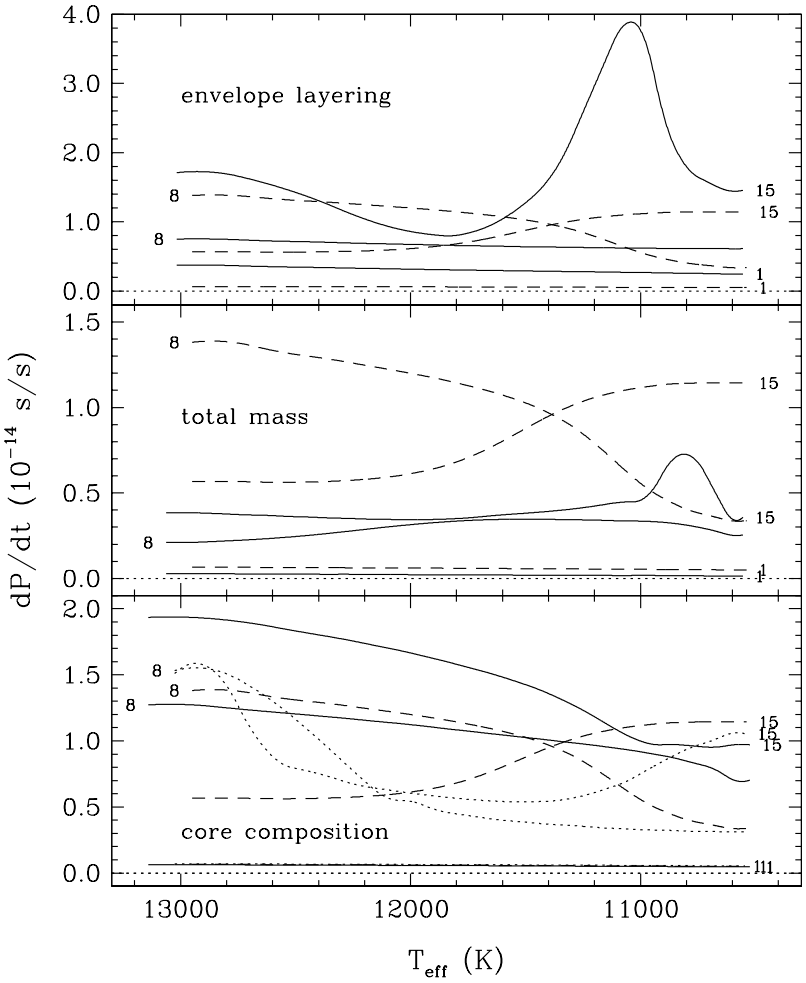

Fig. 14. Effects of varying the envelope layering, the total mass, and the core composition on the rates of period change for representative dipole g-modes ($k = 1$, 8, and 15) in evolving ZZ Ceti star models.

energy conservation equation and the energy transfer equation, are thus called upon at the outset. After linearization, one ends up with a system of 6 linear differential equations with 6 dependent *complex* eigenfunctions.[4] As compared to the adiabatic approximation (which leads to a set of 4 linear equations

[4] This is true for models in which only radiative (and conductive) transport is taken into account, although the one extreme treatment of convection that has been used most often for white dwarfs, the so-called frozen convection approximation, does not require additional equations. A time-dependent version of convective transport does, however.

with *real* variables), the full approach becomes a much more complicated problem from a numerical point of view. This is the price to pay, however, to verify if a pulsation mode is excited or not in a stellar model. Likewise, the full nonadiabatic approach is necessary to understand why a pulsating star pulsates, and to map instability strips, among other things.

In the full nonadiabatic version, the eigenfrequency σ of a mode is a complex number and its temporal dependence takes on the form,

$$e^{i\sigma t} \; = \; e^{i(\sigma_R + i\sigma_I)t} \; = \; e^{i\sigma_R t} e^{-\sigma_I t} \quad , \tag{20}$$

where σ_R is the (angular) oscillation frequency of the mode, and σ_I (also expressed in rad s^{-1}) is directly related to the so-called e-folding time of the mode defined by $\tau_e = -1/\sigma_I$. (In some references, the term "growth rate" is also defined by the expression $\gamma = -\sigma_I/\sigma_R$). When σ_I is positive, the amplitude of the initial perturbation decays according to equation (20), and the mode is said to be stable, damped, or not excited, and the mode is not expected to be observable. Conversely, when σ_I is negative, the amplitude of the initial perturbation blows up exponentially (this is linear theory), and the mode is said to be unstable, driven, or excited. Such a mode may grow to an observable amplitude in a real pulsator. Note that, quite generally in stellar models and especially for low-order modes, $|\sigma_R| \gg |\sigma_I|$, which partly explains why the adiabatic approximation is usually justified for computing oscillation frequencies (periods) at a sufficient level of accuracy.

In nonadiabatic pulsation theory, one very useful concept is that of a "work integral" which may be evaluated from the (nonadiabatic) eigenfunctions after the solution of the eigenvalue problem has been obtained. In a way similar to the weight function discussed in Subsection 4.5 above, the integrand of the work integral indicates which regions of a stellar model contribute to the driving of a pulsation mode, and which regions contribute to damping. The integrand of the work integral may be written in the form,

$$\frac{dW}{dM_r} \; = \; \frac{\pi}{\sigma_R} \mathrm{Re} \left\{ \frac{\delta T^*}{T} \left[\delta\epsilon_{\mathrm{N}} - \delta \left(\frac{1}{\rho} \boldsymbol{\nabla} \cdot (\boldsymbol{F}_R + \boldsymbol{F}_C) \right) \right] \right\} \quad , \tag{21}$$

where the terms have their standard meaning. The nuclear term, $\delta\epsilon_{\mathrm{N}}$, has yet to prove its relevance for pulsating white dwarfs, although it could drive, through the appropriately named ϵ-mechanism, short-period g-modes in some models of GW Vir stars with residual He shell burning according to [37] (and see also [12]). Short period pulsations of the type have yet to be discovered in GW Vir stars, however, and it is now generally acknowledged that the modes observed in the pulsators of the kind are driven by the so-called κ-mechanism involving the modulation of the radiative flux $\boldsymbol{F_R}$ around an opacity bump in the envelope (see, e.g., [31], and references therein). The ϵ-mechanism, this time based on H shell burning, could also drive short-period (40−125 s) g-modes in some low-mass DAO white dwarfs which result from post-EHB evolution as demonstrated by [9]. In this context, the heavy solid segment of

the dotted curve shown in Figure 1 indicates the predicted instability region. No low-mass DAO white dwarf has been found to pulsate yet (see, in particular, [22]), but these objects are quite rare and the jury is still out about the possibility. This is particularly true in the light of the recent study of [20] who have shown that the presumed post-EHB DAO white dwarfs studied for variability by [22] are, in fact, post-AGB white dwarfs. In the cases of the V777 Her and ZZ Ceti stars, residual shell burning is completely negligible and the ϵ-mechanism cannot operate. Instead, the modulations of both the radiative and convective flux must be taken into account in the driving process as these cooler white dwarfs have developed extensive superficial convection zones that interact with the pulsations. For lack of a better approach, stability studies of white dwarfs of the kind have largely been based on the so-called frozen convection approximation, which consists in neglecting the perturbations of the convective flux. Fortunately, progress has been made recently on this front by implementing, for the first time, an approach based on a time-dependent treatment of convection in a white dwarf context ([15], [33], [42])

The sign of the integrand dW/dM_r indicates if, locally, a region of the star has a stabilizing or destabilizing effect on a mode. If $dW/dM_r < 0$, the region will be short of energy after a pulsation cycle and that energy will be taken from the kinetic energy of the mode. The amplitude of the mode tends then to decrease locally, and the region contributes to damping of the mode. If, on the other hand, $dW/dM_r > 0$, the region ends up with a positive energy increment after a cycle, which is transfered as extra kinetic energy to the mode. The amplitude has then a tendency to grow locally, and the region contributes to driving. The global stability of a mode is determined by summing over the contributions of all regions in a model, and this is the work integral given by,

$$W = \int_0^M \frac{dW}{dM_r} dM_r \quad . \tag{22}$$

If $W < 0$, damping dominates over driving and the mode is globally stable. Conversely, if $W > 0$, the mode is globally excited.

6.2 Excitation of pulsation modes in white dwarfs

The phenomenon ultimately responsible for driving pulsation modes in white dwarfs is the partial ionization of the main envelope constituents. Indeed, the K-shell electrons of carbon and oxygen ionize and then recombine during the excursion around the bend in the GW Vir phase of the evolution of a H-deficient, post-AGB star, helium recombines in the stricly cooling phase of a He-atmosphere white dwarf corresponding to the V777 Her regime, and so does hydrogen in the even cooler phase of a H-atmosphere star corresponding to the ZZ Ceti regime. Both the recombination of helium and carbon contribute to the excitation of g-modes in models of cooling Hot DQ stars. In

each case, partial ionization leads to a very important increase of the envelope opacity, and this tends to choke the outgoing energy flux. In the case of V777 Her models, and even more so in Hot DQ models and ZZ Ceti stars, the opacity bump becomes so large that a superficial convection zone develops as a result of the buildup of a superadiabatic temperature gradient, and this significantly affects the mechanics of the actual process responsible for the excitation of pulsation modes. Convective energy transport must then be taken into account in addition to the usual radiative channel. Figure 15 illustrates some opacity profiles and convective flux profiles in the envelopes of typical models of pulsating white dwarfs. The monotonic increase of the opacity maximum with decreasing effective temperature (GW Vir, V777 Her, Hot DQ, ZZ Ceti) is noteworthy.

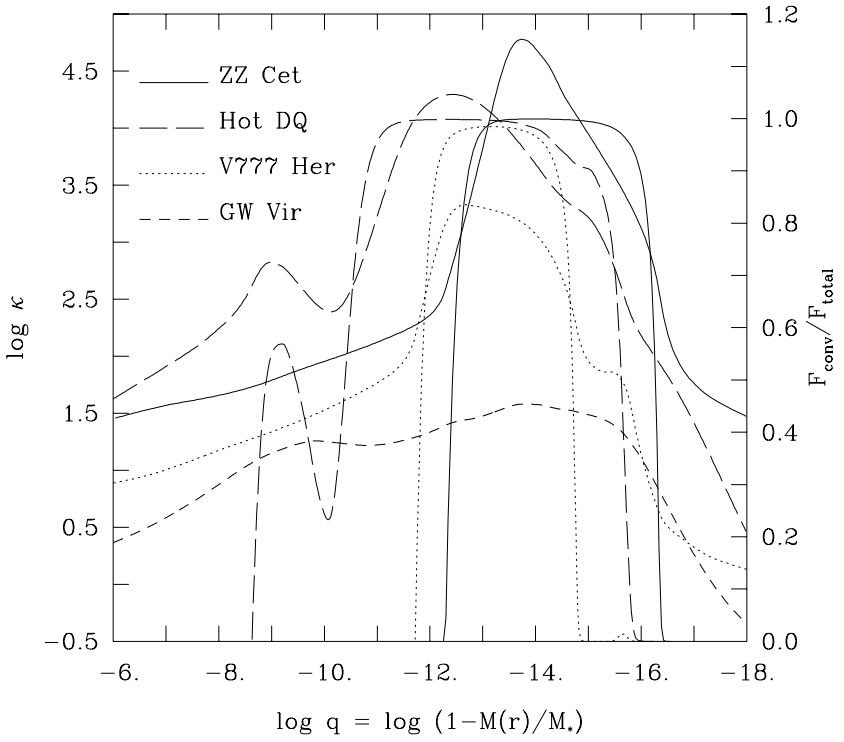

Fig. 15. Opacity profiles (heavy curves) in the envelopes of representative models of the four types of pulsating white dwarfs. The ratio of the convective to total flux is also plotted (thin curves), except for the GW Vir model in which there is no convection.

Figure 16 illustrates the details of the driving/damping region in a representative model of a GW Vir pulsator. In this diagram, the abscissa corre-

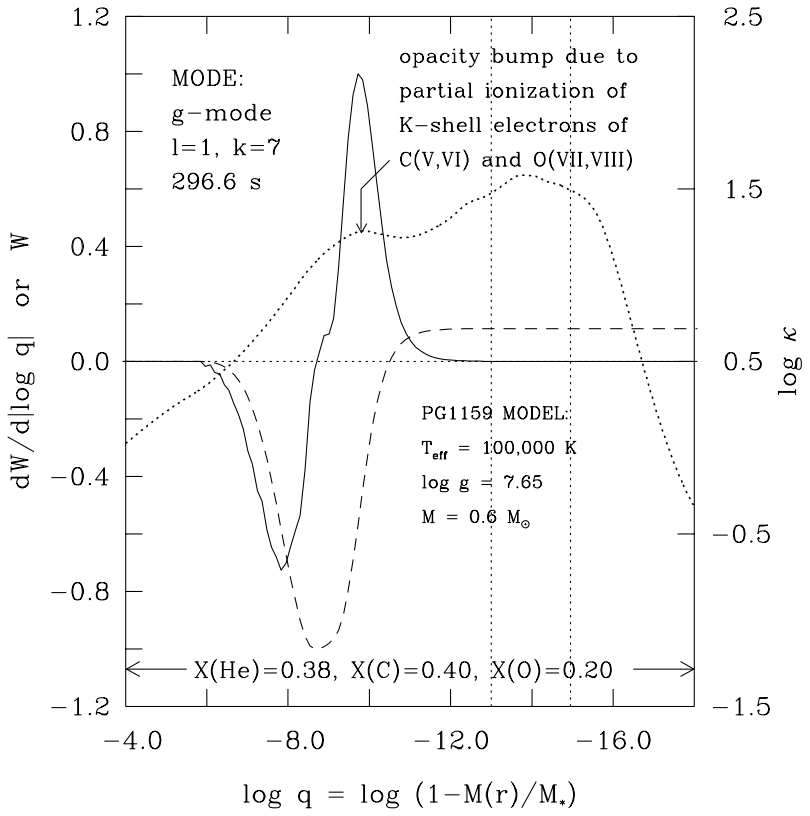

Fig. 16. Details of the driving/damping process for a typical g-mode excited in a model of a GW Vir star.

sponds to the logarithm of the fractional mass above the depth of interest, the same as used in our Figure 4 above, for example. On this scale, the center of the star would be at a log q value of 0.0.[5] However, because all of the "action" in terms of driving/damping is going on only in the outer envelope of the model, it is appropriate to emphasize only that part of the star in the plot. The first vertical dotted line when moving into the star from the right gives the location of the photosphere (corresponding to optical depth $\tau_R = 2/3$), and the second vertical dotted line indicates the position of the base of the atmosphere ($\tau_R = 100$). The dotted curve shows the profile of the Rosseland opacity – to be read on the right-hand ordinate axis – as a function of depth.

[5] Contrary to most asteroseismologists who work on nondegenerate stars, we prefer in the white dwarf field to use log q as the abcissa in this type of diagram instead of the temperature. This is because elements such as H, He, or C do not ionize at the known "canonical" values of the temperature in white dwarfs because of pressure effects on the ionization balance.

One can notice two maxima in the opacity profile: the larger one nearer to the surface is the usual "Z-bump", while the deeper one corresponds to the partial ionization of the K-shell electrons in carbon and oxygen. Note that the envelope chemical composition of this model is uniform and made of a mixture of He, C, and O in proportions typical of those observed in the atmospheres of real GW Vir pulsators ($X(\mathrm{He}) = 0.38$, $X(\mathrm{C}) = 0.40$, $X(\mathrm{O}) = 0.20$, $Z = 0.02$).

Of the many g-modes found excited in this model, a representative one with indices $k = 7$ and $l = 1$ has been singled out. It has a period of 296.6 s. For this particular mode, the solid curve shows the arbitrarily normalized integrand $\mathrm{d}W/\mathrm{dlog}\, q$ of the work integral discussed in Subsection 6.1 above. This derivative is obtained with respect to the independent variable $\log q$ instead of M_r as given in equation (21), but it will be understood that this boils down to an arbitrary choice for the abscissa variable. As discussed previously, a negative value of $\mathrm{d}W/\mathrm{dlog}\, q$ at a given depth means that the mode is locally damped. Conversely, a positive value implies that the mode is locally driven. The dashed curve is related and illustrates the running work integral W, from left to right, i.e, from the center toward the surface of the model. This quantity is also arbitrarily normalized. A final positive value of the work integral at the surface – as is the case illustrated here – means that the mode is globally excited and is potentially observable. Conversely, a negative value of the work integral at the surface would imply that the mode is globally damped and should not be seen.

Figure 16 clearly reveals that maximum driving corresponds to the opacity bump associated with the partial ionization of the K-shell electrons in C and O. Of prime interest, the work integral curves bear the telltale signature of a classic κ-mechanism. Note that there is no contribution to the driving/damping process coming from the region associated with the higher maximum in the opacity profile in the figure, and this is simply because it is located in the atmospheric layers where there is practically no mass.

Figure 17 is similar, but it refers to a representative model of a V777 Her pulsator. It has the same format as the previous plot, except for the addition of the profile of the ratio of the convective to the total flux, F_c/F_t (long-dashed curve). The g-mode with $k = 7$ and $l = 1$ is again excited in this model and was picked as an illustrative example. Here, the envelope is constituted of pure He, and one can observe a large opacity peak caused by the partial ionization of He I near the photosphere and, more importantly, that of He II in the deeper layers where the opacity reaches a maximum around $\log q \sim -12.7$. The two partial ionization zones of helium are practically fused together in this 25,000 K white dwarf model because of pressure effects. This leads to the formation of a significant convection zone extending from above the photosphere well into the driving/damping region below. Quite importantly, this convection zone carries up to 98% of the total flux at maximum efficiency.

One can notice from the figure that maximum driving does not occur at the depth where the opacity reaches its maximum value, but somewhat below.

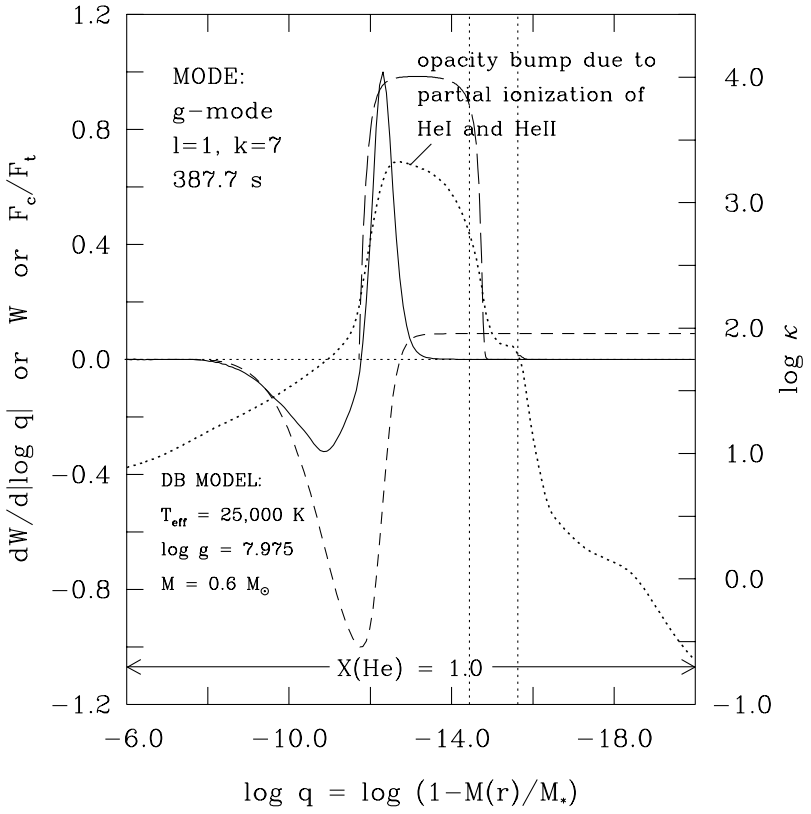

Fig. 17. Details of the driving/damping process for a typical g-mode excited in a model of a V777 Her star.

Also, driving ($\mathrm{d}W/\mathrm{d}\text{—}\log q\text{—} > 0$) is concentrated in a broad region near the base of the convection zone, a region in which the fraction of the flux carried by convection varies from zero at the base to its maximum value near the top of that region. Contrary to GW Vir pulsators then, convection has a significant role to play in the pulsation of V777 Her white dwarfs. Its presence in the driving region implies that it is not the classic κ-mechanism that is at work in these stars because that mechanism only operates in a purely radiative environment.

A very similar situation is encountered in ZZ Ceti stars, but the physical conditions are even more extreme in these cooler objects than in V777 Her pulsators. This is illustrated in Figure 18 which now refers to the case of a typical model of a pulsating DA white dwarf. Taking into account the different scale used for the opacity axis as compared to the previous figure for example, one can notice the huge opacity peak in the pure H envelope of this model. This bump is due to the partial ionization of neutral hydrogen. It is appropriate

to recall in this context the gradual increase of the opacity maximum from Figure 16 to Figure 18 (as described as well in Fig. 15).

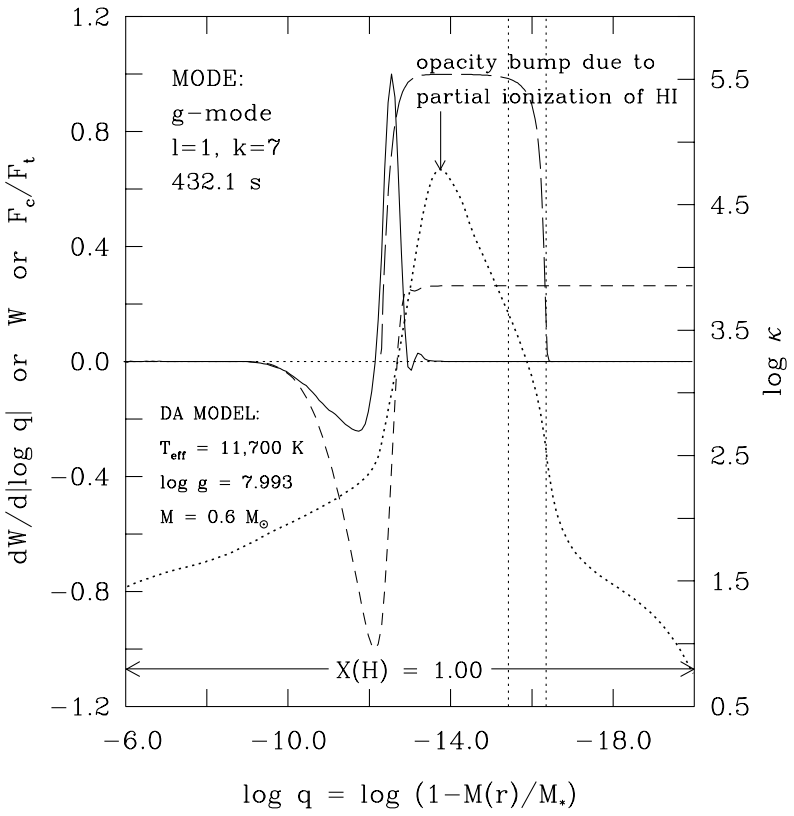

Fig. 18. Details of the driving/damping process for a typical g-mode excited in a model of a ZZ Ceti star.

The convection zone associated with this opacity feature extends all the way from the photosphere to the base of the driving region. It is more important than in the DB model in the sense that up to 99.9% of the total flux can be carried convectively in this zone. The driving region is again concentrated at the base of the convection zone, but in a narrower domain than in the V777 Her case. Moreover, maximum driving is clearly more separated from maximum opacity than in the previous case. We can see, from both Figures 17 and 18, that pulsation driving in V777 Her and ZZ Ceti stars is intimately associated with the physical conditions near the base of the superfical convection zone.

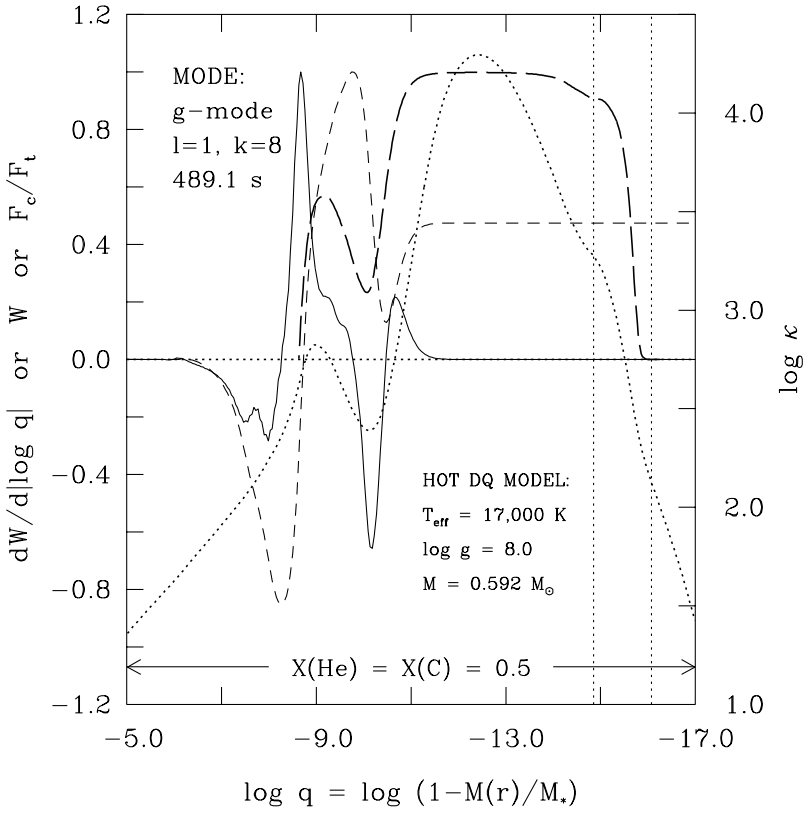

Fig. 19. Details of the driving/damping process for a typical g-mode excited in a model of a Hot DQ star.

The physics is essentially the same for the Hot DQ model depicted in Figure 19, although the mixed envelope composition leads to two distinct regions of driving in the model. The envelope composition is again assumed to be uniform, and is made of a mixture defined by $X(\mathrm{C}) = X(\mathrm{He}) = 0.5$. The maximum in the opacity profile, located at $\log q \simeq -12.4$ is caused by the partial ionization of He II, CIII, and CIV in the envelope mixture. The secondary maximum, located at $\log q \simeq -9.0$ is caused instead by the partial ionization of CV and CVI. Those two opacity bumps are "active" in the sense that both contribute to the driving/damping process. It can be observed in the figure that the regions on the descending side (going in from the surface) of an opacity bump contribute locally to driving, while the deeper adjacent zones, where the opacity decreases to relatively low values, contribute instead to damping. In the present model, the two opacity bumps are relatively close to each other and are part of a single convection zone. The damping region

between the two bumps is relatively narrow and the overall work integral comes out positive for this particular mode.

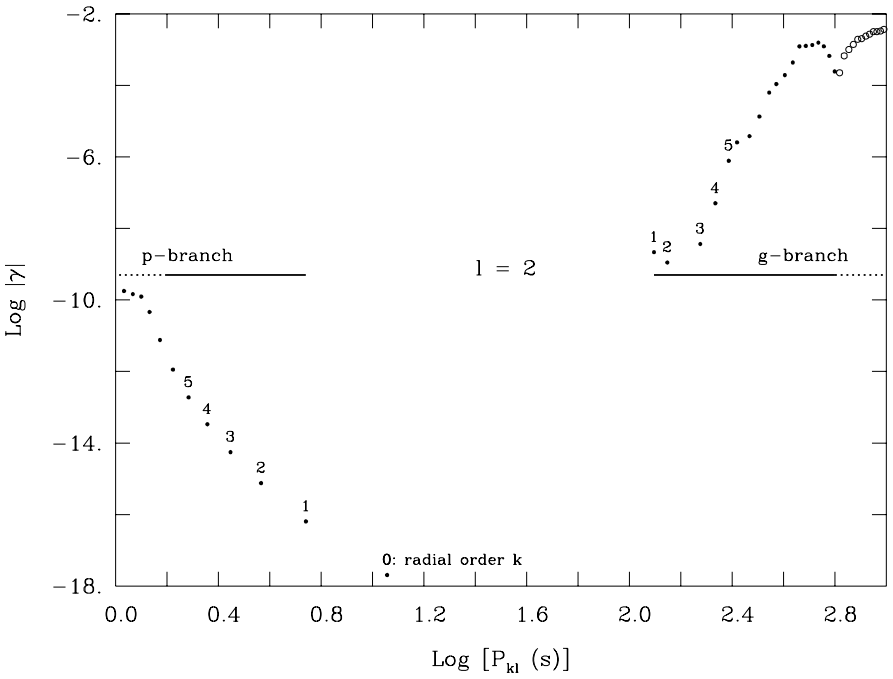

Fig. 20. Absolute value of the growth rate, $\gamma = -\sigma_I/\sigma_R$, as a function of period for the family of quadrupole modes with periods in the range from 1 s to 1000 s as computed on the basis of our reference ZZ Ceti star model. The excited (stable) modes are indicated by the small filled (large open) circles. The format is similar to that of Fig. 7 above, and the modes considered are the same.

It should be noted that, while the classic κ-mechanism is at work in GW Vir pulsators, the presence of convection in the driving/damping regions of V777 Her, Hot DQ, and ZZ Ceti models implies that the detailed excitation process in those pulsators should be associated with the so-called "convective driving" mechanism first proposed by [6]. A more detailed description of the interaction occuring between pulsations and convection in these cooler white dwarfs is provided by [15], [33], and [42]. In addition, and for completeness, it is worthwhile to recall that low-order p-modes, including radial modes, are expected to be excited in some DB and some DA white dwarfs according to [38]. And indeed, the mechanism able to drive low-order g-modes in these cooler white dwarfs ought to work also for low-order p-modes. This is also what we find in Figure 20 which illustrates the behavior of the growth rate for the family of quadrupole modes already considered above for a representative ZZ

Ceti star model. Except for the higher-order g-modes (identified with large open circles), all of the modes are predicted to be excited, including all of the low-order p-modes considered. However, short period p-mode pulsations have yet to be found in white dwarfs, and this has remained a small mystery. We note that the growth rates are significantly lower for the illustrated p-modes compared to the g-modes, but other explanations may be necessary (see, e.g., [17]).

6.3 Expected instability strips for white dwarfs

Nonadiabatic calculations are essential for understanding the very existence of a given type of pulsating star. They are also required to map the instability strips in the HR diagram. Comparisons of "nonadiabatic observables" with predictions of nonadiabatic theory are of fundamental importance for inferring the thermal properties and the evolutionary status of pulsating stars. Among such observables one may identify the boundaries of an instability domain for a given family of pulsators, and the range of excited periods along with the periods themselves in individual stars. We illustrate these concepts in this subsection with the help of examples taken from white dwarf asteroseismology.

Figure 21 shows the predicted ranges of periods for excited dipole ($l = 1$) modes computed from GW Vir models with $\log g$ and $T_{\rm eff}$ values culled from the evolutionary calculations of [37]. These ranges are shown as functions of the effective temperature for an evolving model with $M = 0.56\ M_{\odot}$ (filled circles) and for another one with $M = 0.60\ M_{\odot}$ (open circles). Along these evolutionary tracks, equilibrium structures were pulsated and the resulting excited modes are represented by small circles. The envelope composition of these structures is a representative mixture for a GW Vir star specified by $X(\mathrm{He}) = 0.38$, $X(\mathrm{C}) = 0.40$, $X(\mathrm{O}) = 0.20$, $Z = 0.02$ in units of mass fraction, the same as that used in a previous experiment above. Each circle has a size that gives a logarithmic measure of the modulus of the imaginary part of the complex eigenfrequency, i.e., $|\sigma_I|$. The bigger the circle, the more unstable the mode. These predicted period ranges reproduce very well the results of [37]. In particular, one can note that the $0.60\ M_{\odot}$ models show two distinct instability phases along their evolutionary track, while the $0.56\ M_{\odot}$ models show a single one. The modes depicted in the figure are excited through the C/O κ-mechanism; the ϵ-mechanism was not considered in these computations.

Another example is provided in Figure 22, which displays the locations of theoretical instability strips for evolving $0.6\ M_{\odot}$ white dwarf models with different envelope compositions. Along with the usual V777 Her (pure He) and ZZ Ceti (pure H) instability strips, one can recognize the red edge of the pulsating pure C envelope white dwarf models. In fact, the pure C instability strip extends all the way up to the GW Vir regime as described at length in [32]. On the other hand, models with a mixed He and C envelope composition can also pulsate, but in different temperature intervals. For instance, Figure

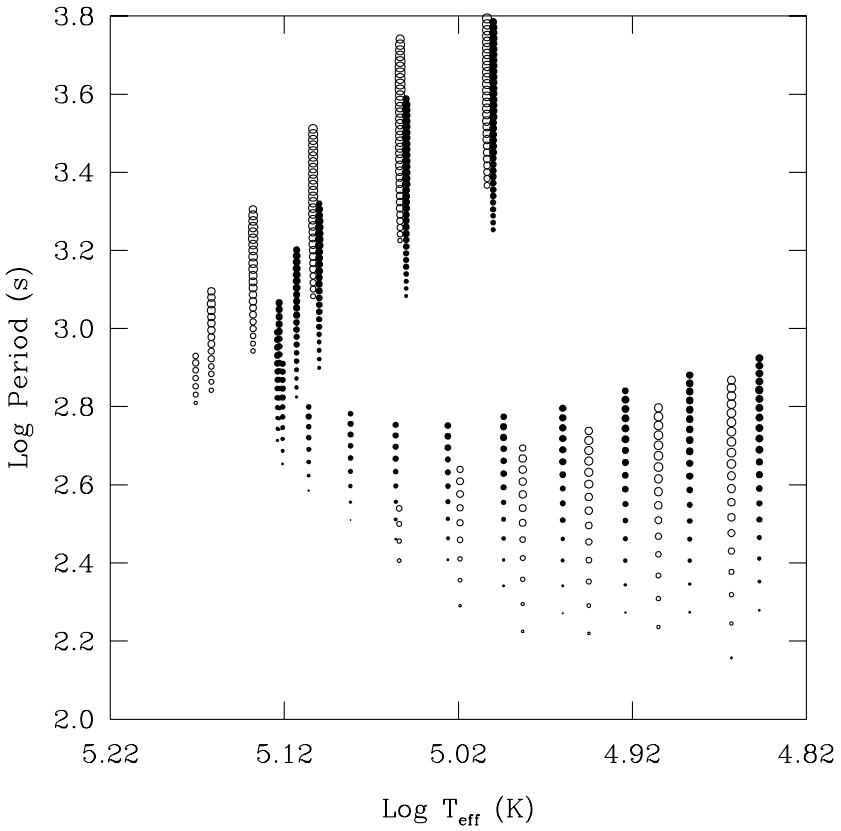

Fig. 21. Predicted ranges of periods for excited dipole modes computed from GW Vir models culled from two different evolutionary sequences: $M = 0.56\ M_{\odot}$ (filled circles) and $M = 0.60\ M_{\odot}$ (open circles).

22 illustrates an instability strip between the V777 Her and the ZZ Ceti domains associated with white dwarf models with a mixed envelope composition specified by $X(\mathrm{He}) = X(\mathrm{C}) = 0.5$, as appropriate for Hot DQ stars. Naively, one could have expected to find such a strip in between the pure C and pure He strips, but structural differences in the mixed envelope composition models explain why this is not so.

Nonadiabatic asteroseismology can also be used to infer properties of individual pulsators or of a class of pulsators as a whole. An example of that comes from ZZ Ceti stars and concerns the calibration of the mixing-length theory in the layers where driving occurs, in effect providing a measurement of the depth of the convection zone in such stars. This becomes possible because pulsational instabilities first set in along the evolutionary track of a cooling H-atmosphere white dwarf when the base of the convection zone that develops due to hydrogen recombination reaches a certain critical depth. When

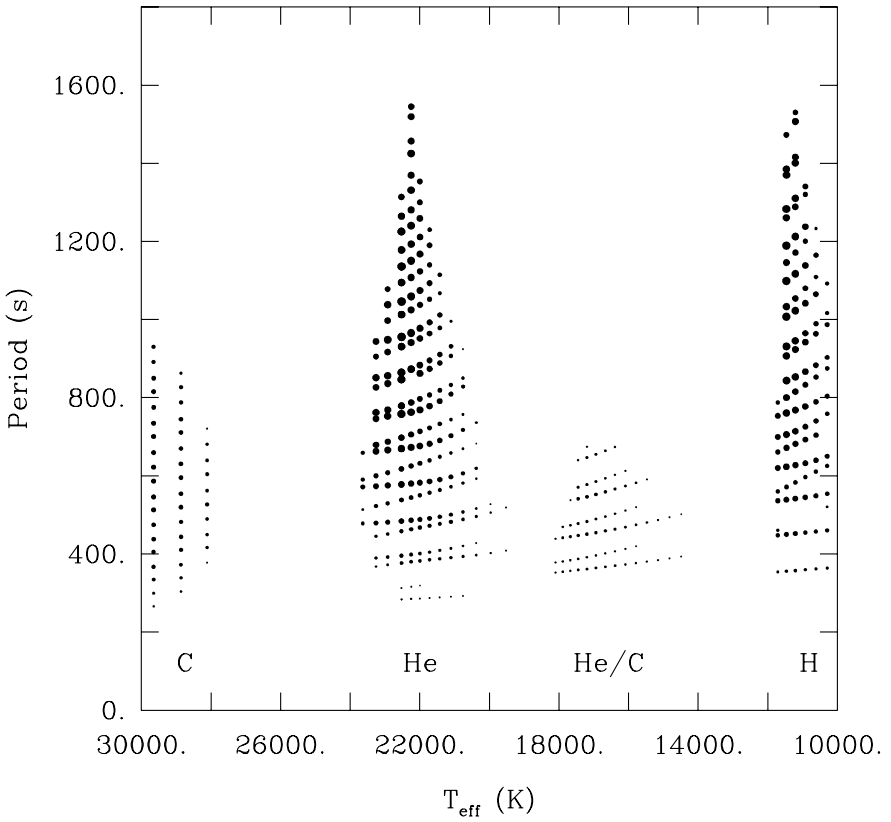

Fig. 22. Predicted spectra of excited g-modes computed from four distinct evolutionary sequences, each characterized by a total mass of 0.6 $M_{\odot}$, but with a different envelope composition: pure C, pure He, $X(\mathrm{He}) = X(\mathrm{C}) = 0.5$, and pure H, from left to right.

this occurs, the star enters the blue edge of the instability strip. In this context, it was mentioned above that the driving region in a ZZ Ceti pulsator is essentially located at the base of the H convection zone, so there is a direct connection between the effective temperature at the blue edge and the depth of the H convection zone. Since convection is still modeled in terms of the mixing-length theory in white dwarfs, a comparison of the empirical blue edge of the strip with that provided by nonadiabatic calculations may be used to infer the convective efficiency at the base of the convection zone, i.e., in the driving region.

The principle of the method is exposed in Figure 23. That figure displays the instability domain in the $\log g - T_{\mathrm{eff}}$ diagram for the ZZ Ceti stars. The positions of the pulsators are indicated by the filled circles, while those of the nonvariable stars are given by the open circles. The error cross in the lower left

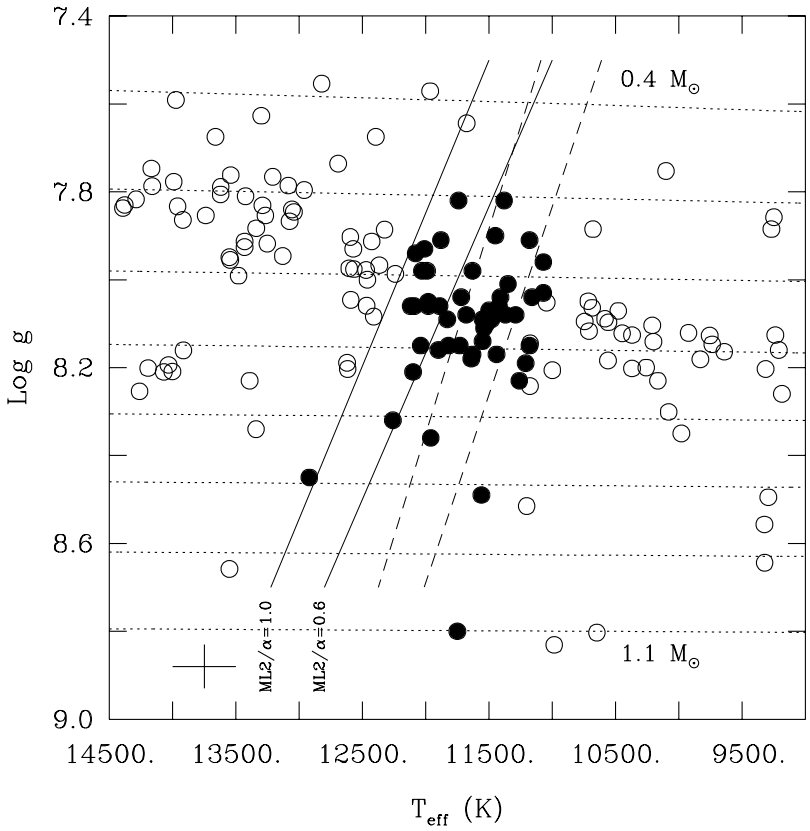

Fig. 23. Calibrating the mixing-length theory in ZZ Ceti stars by matching the empirical blue edge of the instability strip with the predicted blue edge computed under the assumption of various convective efficiencies (see text).

part of the figure gives the typical uncertainties on the atmospheric parameters. The dotted curves illustrate evolutionary tracks for H-atmosphere white dwarfs of different masses, from 0.4 $M_\odot$ above to 1.1 $M_\odot$ below in steps of 0.1 $M_\odot$. The solid curve on the left (right) gives the location of the theoretical blue edge assuming a convective efficiency given by the so-called ML2/α=1.0 (ML2/α=0.6) version of the mixing-length theory used in the construction of the equilibrium models employed in the nonadiabatic calculations. These theoretical boundaries were obtained using the instantaneous convective response hypothesis, which is certainly justified since the convective turnover timescale is much smaller than the periods of excited modes in these models at the blue edge. One can see that the ML2/α=1.0 version provides a rather good match to the empirical data. In contrast, models computed using the same two versions of the mixing-length theory (dashed lines), but within the framework of the frozen convection approximation fare a lot worse at matching the

empirical blue edge. While this needs to be refined, the approach probably remains the best way for calibrating the mixing-length theory in white dwarfs as appropriate for the deep envelope regions.

7 Example of a Successful Asteroseismological Exercise

We end our presentation by providing an example of an asteroseismological exercise carried out succesfully for the pulsating white dwarf GD 165, with the aim of deriving the global structural parameters of the star on the basis of period-matching algorithms. This is carried out within the framework of the adiabatic approximation, but nonadiabatic considerations are also presented in a complementary discussion.

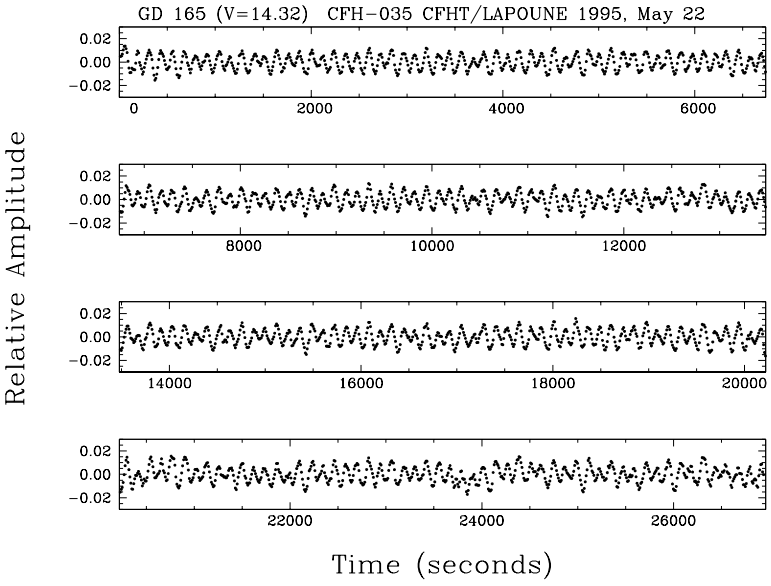

Fig. 24. Representative broadband optical light curve obtained on GD 165 using the CFHT/LAPOUNE combination. The amplitude is expressed in terms of residual intensity relative to the mean brightness of the star. Each plotted point represents a sampling time of 10 s.

7.1 Observations and period extraction procedure

The pulsating white dwarf GD 165 ($V = 14.32 \pm 0.01$) is one of those "simple" low-amplitude pulsators found in the hotter region of the ZZ Ceti instability strip which tend to show stable and relatively uncomplicated light curves. Its time-averaged atmospheric properties place it at $T_{\rm eff} = 11{,}980$ K and $\log g =$

8.06 in the spectroscopic HR diagram (see, e.g., Table 1 of [17]. An analysis of a Whole Earth Telescope (WET) campaign carried out on GD 165 in 1990 May was presented by [2]. The campaign resulted in some 233 h of broadband "white light" photometric data gathered from six different sites using small telescopes. The formal resolution achieved during the campaign was 1.2 μHz, and the duty cycle was 35%. Despite these considerable efforts, the results turned out to be rather disappointing as only three main periodicities could be detected. Furthermore, it was not possible to decide if the fine structure observed in the two largest peaks in the Fourier transform of the light curve was due to triplets or quintuplets. In brief, the exercise was defeated by the low signal-to-noise ratio (S/N) of the observations in regard to the relatively low amplitudes of the modes excited in GD 165.

Table 1. Observed properties of the 13 modes detected in GD 165, assigned rotation coefficients, and inferred rotation period

P(s)	A(%)	$\nu(\mu$Hz)	$\Delta\nu(\mu$Hz)	C_{kl}	$P_{\rm rot}$(h)	ID
120.3202±0.0008	0.1173±0.0052	8311.16±0.05	2.470±0.054			...
120.3559±0.0002	0.5244±0.0052	8308.69±0.01	<2.464±0.032>	0.492	57.27±0.74	f_1
120.3916±0.0006	0.1649±0.0052	8306.23±0.04	2.460±0.040			...
192.5701±0.0015	0.2289±0.0078	5192.92±0.04	2.965±0.058			...
192.6801±0.0015	0.2287±0.0078	5189.95±0.04	<2.937±0.054>	0.399	56.85±1.05	f_2
192.7828±0.0052	0.0683±0.0078	5187.18±0.14	2.766±0.145			...
250.1589±0.0066	0.0574±0.0051	3997.46±0.11	2.670±0.268	0.487	53.37±5.36	f_3
250.3261±0.0154	0.0253±0.0051	3994.79±0.25				...
114.2344±0.0015	0.0446±0.0043	8753.93±0.12	8.950±0.327	0.084	56.85±2.08	f_4
114.3513±0.0039	0.0174±0.0043	8744.98±0.31				...
146.3160±0.0011	0.0447±0.0060	6834.53±0.16	3.915±0.394	0.156	59.88±6.02	f_5
146.3998±0.0077	0.0195±0.0060	6830.61±0.36				...
168.1912±0.0074	0.0272±0.0059	5945.62±0.26	...	...	...	f_6

Another broadband photometric campaign on GD 165 was carried out by two of us using the CFHT/LAPOUNE combination in 1995 May. The light curve of GD 165 was sampled for a total of 27.8 h over six consecutive nights. The formal resolution achieved was 2.2 μHz and the duty cycle was equal to 22%. The conditions on Mauna Kea during that run were superb as can be appreciated from the sample light curve shown in Figure 24. Because of the much improved sensitivity achieved during the CFHT campaign, eight statistically significant peaks were detected as can be seen in Figure 25

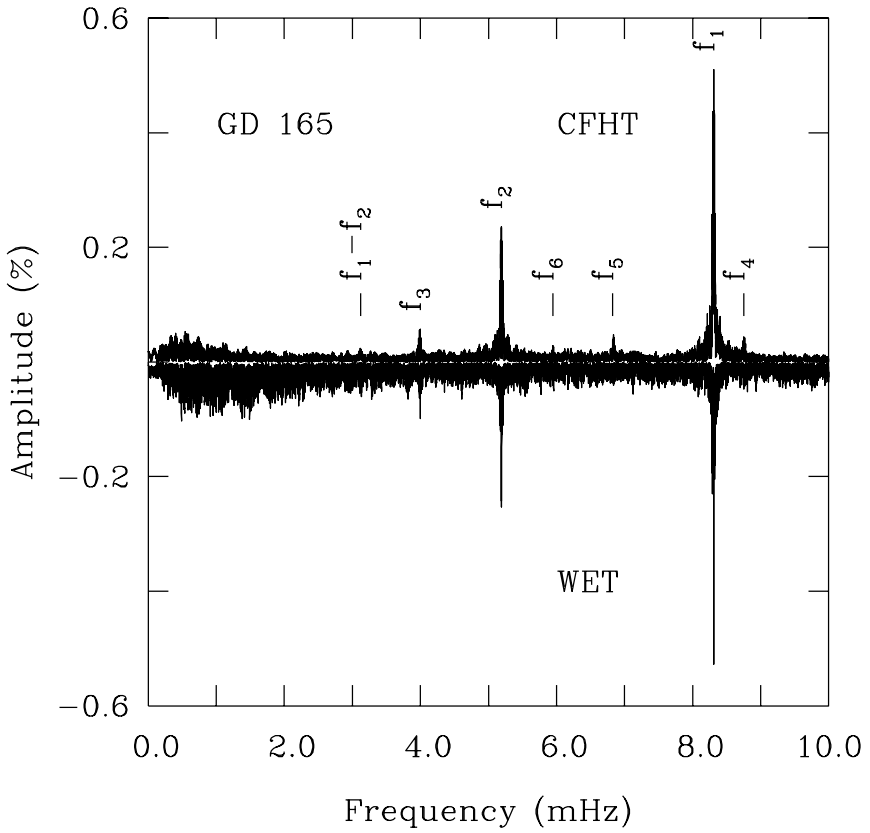

Fig. 25. Comparison of the Fourier amplitude spectrum of the light curve of GD 165 obtained 1) during the 1995 CFHT run (upper curve), and 2) during the 1990 WET campaign (lower curve plotted upside down).

displaying the Fourier amplitude spectra of the two campaigns in the 0−10 mHz bandpass (the $f_1 + f_2$ nonlinear frequency peak is present in the CFHT data, but it falls outside the range of frequency considered in Fig. 25). Standard techniques (Fourier transforms, least-square fits to the light curve, and prewhitening) were used to extract the frequencies (periods) present in the light curve of GD 165. Excluding the nonlinear frequency peaks $f_1 - f_2$ and $f_1 + f_2$ which are not independent modes, a total of 13 modes were uncovered out of six main peaks – identified as f_1 through f_6 in Figure 25 – which include two triplets, three doublets, and a singlet. The first four columns of Table 1 summarize the results of the frequency extraction exercise. It should be noted that the uncertainties on the periods P, the amplitudes A, and the frequencies $\nu = 1/P$ have been estimated with the formalism proposed by [29]. Except for the 146.3998 s component which has a 3.3σ amplitude, the other modes have amplitudes above the 4σ criterion preferred by many researchers.

With an output of 13 frequencies (corresponding to 13 independent pulsation modes) uncovered in GD 165, the CFHT campaign constitutes an eloquent demonstration that single site data, contrary to the seemingly widespread belief in the white dwarf community, *can* be superior to multisite efforts. In this connection, the virtue of high S/N seems to have been often forgotten by many in the past.

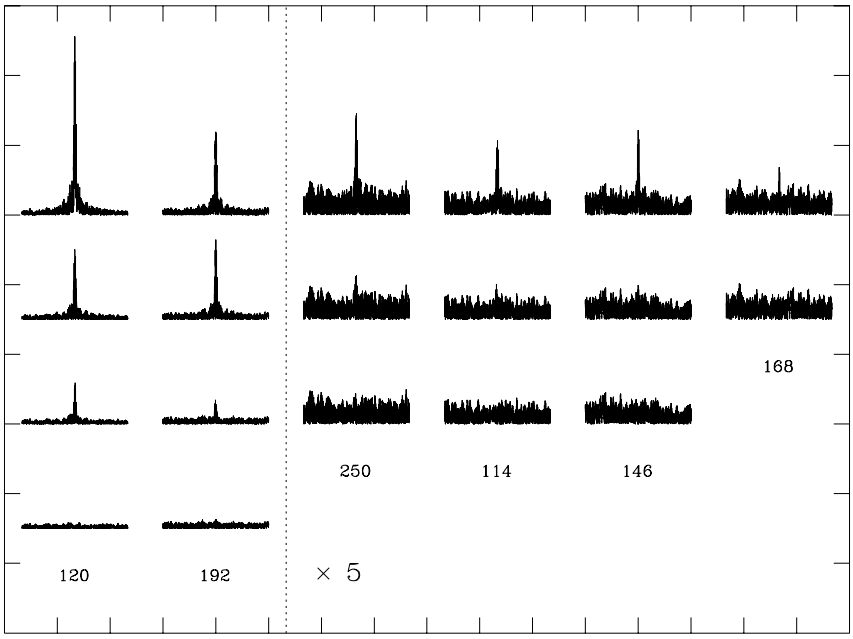

Fig. 26. Prewhitening sequences for each of the six main frequency peaks detected in the Fourier transform of the CFHT light curves on GD 165. One tick mark in abscissa corresponds to 1 mHz, and one in ordinate to 0.2%.

Figure 26 shows the prewhitening sequences (from top to bottom) for each of the six significant peaks that appear in the Fourier amplitude spectrum. The segments of the Fourier transform are displaced, both vertically and horizontally, for visualization purposes. Each column illustrates, from top to bottom, the prewhitening sequence obtained for a given peak identified by its approximate central period (in s). One can distinguish two triplets, three doublets, and one singlet. It is very likely that there are multiplet components in the doublets and the singlet that have not been detected because their amplitudes are smaller than the detection level. Figure 27 provides an interesting zoomed-in view on the 120 s (f_1) complex. Note the very low level of noise in the CFHT data as illustrated by the lower curve. Given the observed spacings

between the frequency components within given multiplets (see column 4 of Table 1), this fine structure is best interpreted as rotational splitting due to slow rotation of the star. This is used below to estimate the rotation period of GD 165, once a convincing seismic model has been found for it.

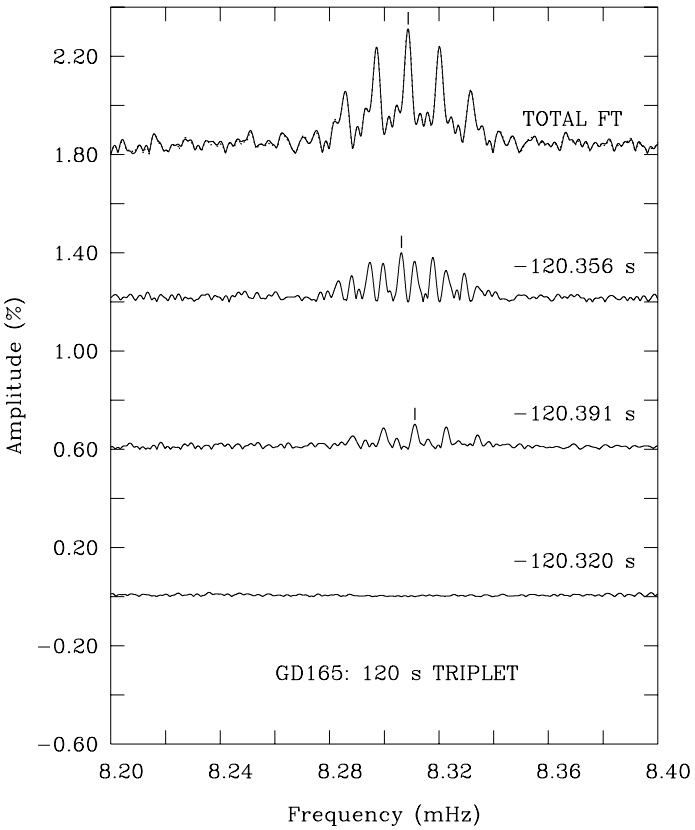

Fig. 27. Prewhitening sequence for the dominant 120 s structure.

7.2 Search for the optimal model in parameter space

For the comparison of the period data with periods computed from spherical models (as usual in the field), it is necessary to assign a priori the $m = 0$ components of multiplets to the unperturbed periods. This leads to some ambiguities, especially for multiplets with an even number of detected components, but it should be recalled that, at the level of accuracy with which periods can be matched with current models of white dwarfs, this does not

pose a significant problem, given that the period differences between multiplet components are very small. Hence, out of the 13 frequency components extracted from the light curve of GD 165, only six are useful for comparison with *spherical* models. These are the six periods identified by f_1 through f_6 in Table 1. Given this set of six periods, a search for a suitable model in parameter space was carried out along the lines pioneered by [5] and further developed by [10].[6]

The technique relies on a double-optimization scheme that, first, best fits the six observed periods (denoted $P_{\rm obs}$ in what follows) with six periods (denoted $P_{\rm theo}$) belonging to the spectrum of a given model (note that the match might be quite poor if the model has properties quite different from those of the real star) and, second, searches for the best-matching model in parameter space. No a priori mode identification is imposed on the observed periods, except that they have to belong to degree index $l = 1$ or $l = 2$ in keeping with what is known about identified modes in white dwarfs. For a given model, theoretical periods are computed in a window that encompasses the range of observed periods for modes with l =1 and 2. For the reasons mentioned above, sufficiently accurate periods may be computed in the adiabatic approximation, so this is adopted as a major time-saving measure because an adiabatic code (solving a set of four linear differerential equations with real variables) is much faster than its nonadiabatic counterpart (dealing with a set of six linear equations with complex variables and requiring, as input and initial guess, the adiabatic eigenfunctions). The quality of the match between the observed and computed periods is measured quantitatively with a merit function defined by,

$$S^2 = \sum_{i=1}^{N_{\rm obs}} \left(P^i_{\rm obs} - P^i_{\rm theo} \right)^2, \tag{23}$$

where $N_{\rm obs} = 6$ in the present case. The goal of the exercise is to find, if possible, the minimum of S^2 in parameter space and, hopefully, a minimum that identifies a good and credible optimal model. To objectively and automatically carry out this search for the optimal model in parameter space (an exercise in the so-called forward approach in asteroseismology) requires considerable computing resources. Currently, a typical exercise of this kind for white dwarfs necessitates the computations of a few million models and of their period spectra. This is best done on a cluster of dedicated PC's such as CALYS (currently containing 320 nodes) being developed in Montréal, for example.

[6] A better approach would be to use models perturbed by rotation at the outset and attempt to match in the best possible way the 13 periods simultaneoulsy without making a priori assumptions as to the identification of the $m = 0$ components. This has been used successfully in the recent asteroseismological analysis carried out by [41] on the short-period pulsating hot B subdwarf star Feige 48, for example.

To define a full (but static) white dwarf model, it is necessary to specify the surface gravity (or the mass via the mass-radius relation), the effective temperature, the envelope layering, the core composition, and the convective efficiency – for a star such as GD 165 – via a flavor or another of the mixing-length theory. Quite realistic static models of white dwarfs can be computed (as compared to full evolutionary models) since in these cooling bodies the approximate relationship between the local luminosity and integrated mass, $L(r) \propto M(r)$, becomes quite accurate and, thus, may be used to provide an excellent estimate of the luminosity profile. As shown in Figure 42 of [17], the periods of low-order g-modes in ZZ Ceti star models practically do not depend on the choice of the assumed convective efficiency, so it is fully justified to adopt one version of the mixing-length theory and not worry further about it. This is especially justified in a star like GD 165 showing rather short periods in the range from $\sim$114 s to $\sim$250 s, because such periods *have* to be associated with low-order modes. Likewise, very little sensitivity is expected of the periods on the core composition in a highly degenerate star such as GD 165 due to the phenomenon of g-mode migration discussed at some length in Subsection 4.5. In the present asteroseismological exercise, the so-called ML2/α=1.0 version of the mixing length theory was therefore adopted and a pure carbon core was assumed. These parameters were not varied in parameter space.

The question of envelope layering deserves some comments. It is specified not only by the total amount of mass there is in the helium mantle, $\Delta M(\mathrm{He})$, and the total amount of mass there is in the hydrogen outer envelope, $\Delta M(\mathrm{H})$, but also by the actual composition profiles in the transition zones themselves. This is because mode trapping/confinement, which has a very significant effect on the g-mode period spectrum in a white dwarf, is very sensitive to the conditions encountered in the composition transition zones. One standard assumption, based on physics as opposed to using some arbitrary profiles at the composition interfaces, has been to invoque diffusive equilibrium in order to compute the chemical distributions in the transition zones. The experiments reported by [3] have been quite enlightening in this respect, in that they have shown that the assumption of diffusive equilibrium does not hold in GD 165. Indeed, this assumption leads, after a full search in parameter space, to a rather poor optimal model characterized by a merit function of $S^2 \simeq 140.7$, a value that is not at all impressive compared to those that have been reached in other pulsating white dwarfs.

The optimal model found by [3], although giving a poor match to the six periods observed in GD 165, still suggested the presence of a rather thick hydrogen layer in that star, a result consistent with the earlier independent arguments put forward by [18]. If true, then the assumption of diffusive equilibrium, which is justified at the base of a thin envelope, had to be questioned. Indeed, one could argue that, at the depths corresponding to the base of a rather thick envelope, diffusion may not have had the time to reach equilibrium (the diffusion timescale increases rapidly with increasing depth in

white dwarfs). This proposition was verified explicitly by [3] who carried out detailed evolutionary calculations including diffusion at the composition interfaces. They were able to conclude that diffusive equilibrium is indeed not reached at the composition interfaces in a ZZ Ceti star model with thick hydrogen and helium layers. More importantly for the present purpose, they were able to "calibrate" the steepness of the composition profiles in a model of GD 165, and it is this calibration that is used here in the present example of an asteroseismological exercise.

With the core composition fixed, the convective efficiency chosen, and two transition zone parameters calibrated (H/He and He/C interfaces), the search for the optimal model in parameter space boils down to a 4D exercise in terms of $T_{\rm eff}$, log g, log $\Delta M({\rm He})/M$, and log $\Delta M({\rm H})/M$, still a formidable numerical challenge. To guide the procedure, and to be consistent with the spectroscopic evidence, the search was confined to a range of $T_{\rm eff}$ and a range of log g corresponding to the 1σ "spectroscopic box" defined by the published uncertainties on these atmospheric parameters, i.e., 11,980 $\pm$350 K in effective temperature and 8.06 $\pm$ 0.05 dex in surface gravity. The mass of the helium mantle was allowed to vary in the range $-4.0 \leq \log \Delta M({\rm He})/M \leq -1.5$, and the mass of the hydrogen envelope was allowed to vary in the range $-8.0 \leq \log \Delta M({\rm H})/M \leq -2.0$, with the condition $\Delta M({\rm He})/M > \Delta M({\rm H})/M$.

Some of the results of the search procedure are presented in Figure 28 showing the behavior of the goodness-of-fit function S^2 in terms of isocontours in the log g-$T_{\rm eff}$ domain that was surveyed. Note that each grid point shows the value of S^2 corresponding to the optimized solution in the two other dimensions as well, i.e., in terms of log $\Delta M({\rm He})/M$ and log $\Delta M({\rm H})/M$. It is very interesting to find out that there is a minimum in S^2 corresponding to $T_{\rm eff}$ = 12,055 K and log g = 8.045. There is indeed never any guarantee at the outset that a minimum will be found within the spectroscopic box. This is the kind of consistency that gives credibility to a seismic solution. In terms of its two other defining parameters, the optimal model coming out of the search exercise has a helium layer mass of log $\Delta M({\rm He})/M = -1.634$, and a hydrogen layer mass of log $\Delta M({\rm H})/M = -4.144$. The optimal model is characterized by a merit function of $S^2 = 1.92$, which is excellent for a fit involving six different periods considering the limitations of current models. It is to be noted that the minimum shown in Figure 28 is rather shallow, which suggests that what was found is more a *family* of equally acceptable models, particularly along the "valley" defined by the contours with $S^2 = 2.0$. A detailed analysis is required to assess the statistical significance of the other model members of the family, but the detailed results indicate that they all correspond to the same mode identification. In the rest of this example, focus is put on the optimal model per se.

The search method yields the mode identification (in terms of the indices l and k for spherical models) consistent with the best S^2 value as output. Table 2 summarizes the period match obtained and the mode identification inferred for the optimal model found for GD 165. In the worst case (the 146.316 s

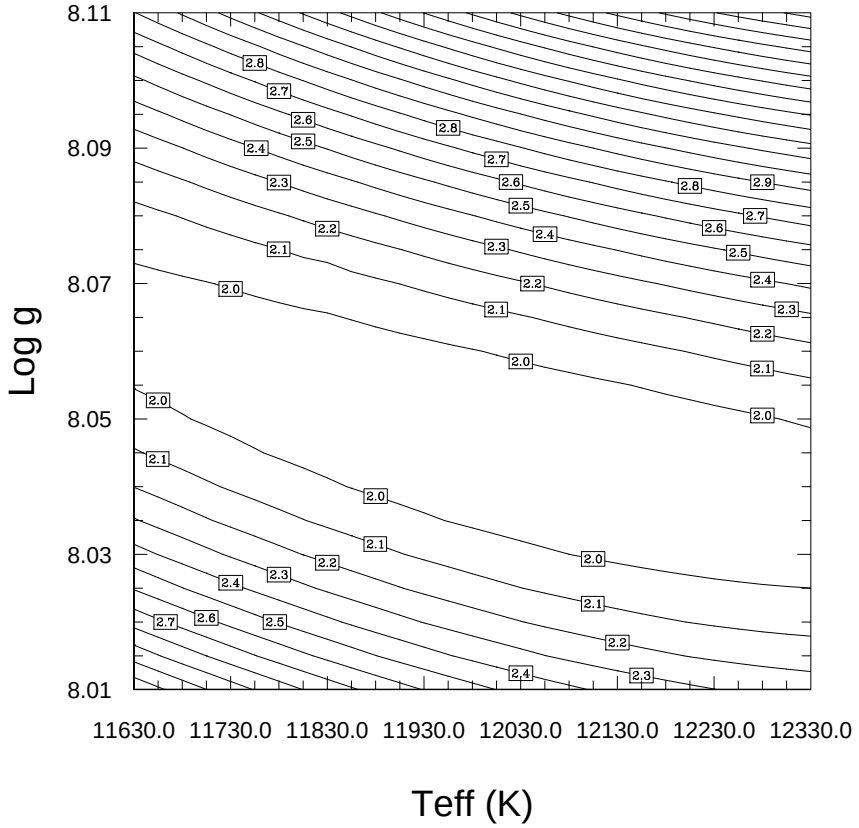

Fig. 28. Contours of the merit function S^2 in the log g-$T_{\rm eff}$ plane.

Table 2. Period fit and mode identification for the optimal model of GD 165

l	k	$P_{\rm obs}$(s)	$P_{\rm theo}$(s)	$\lvert\Delta P\rvert$(s)	C_{kl}	log $E_{\rm kin}$
1	1	120.356	120.143	0.213	0.492	46.553
1	2	192.680	192.770	0.090	0.399	47.517
1	3	250.159	251.015	0.856	0.487	45.318
2	1	...	69.406	...	0.158	46.552
2	2	114.234	114.061	0.173	0.084	47.416
2	3	146.316	145.281	1.035	0.156	45.303
2	4	168.191	168.008	0.183	0.153	45.073
2	5	...	205.824	...	0.147	44.444
2	6	...	224.865	...	0.099	44.334
2	7	...	239.894	...	0.108	44.252
2	8	...	269.077	...	0.151	43.625

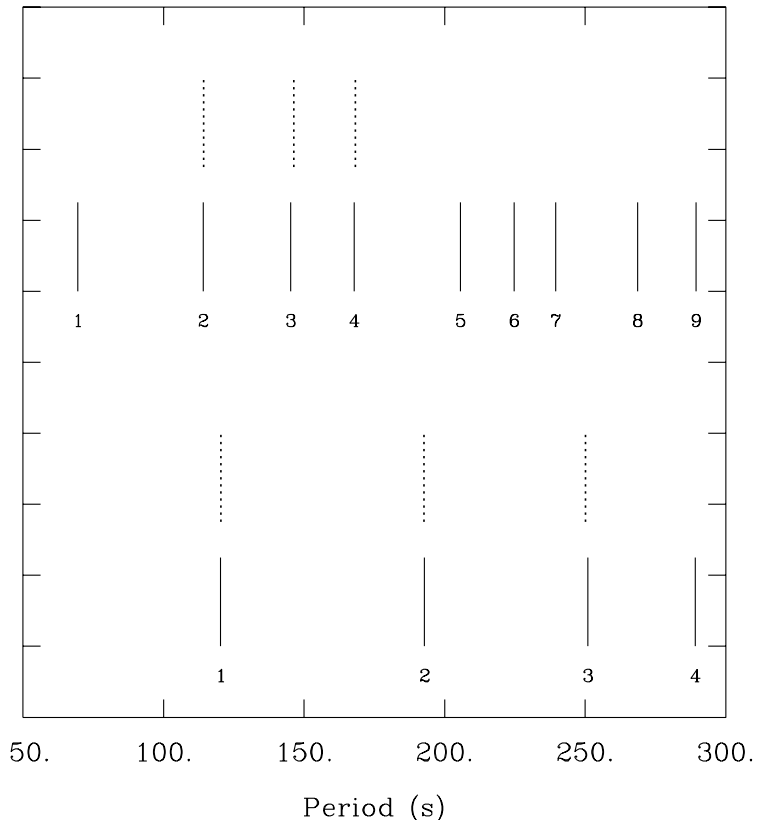

Fig. 29. Comparison of the six observed periods in GD 165 (dashed line segments) with the theoretical g-mode period spectrum of the optimal model (solid line segments). The dipole (quadrupole) modes are illustrated in the lower (upper) half of the plot and the radial order of each mode is indicated.

mode), there is a difference of 1.035 s between the observed period and the theoretical period of the assigned $l = 2$, $k = 3$ mode in the optimal model. Figure 29 provides a graphic representation of this excellent overall fit.

It may be significant that the search exercise has assigned the three largest amplitude oscillations in GD 165 to $l = 1$ modes, and the three smallest amplitude ones to $l = 2$ modes (and see again Fig. 25). This is indeed the expected hierarchy in view of geometrical cancellation effects, but this argument should be used with caution as there are known cases of pulsating stars (including white dwarfs) that show $l = 2$ modes with larger amplitudes than $l = 1$ modes. It is also of interest to point out that the assigned modes in Table 2 have consecutive values of the radial order; from $k = 1$ to $k = 3$ for the dipole modes, and from $k = 2$ to $k = 4$ for the quadrupole modes. This is again circumstantial evidence that adds to the credibility of the optimal model because

nonadiabatic theory (see below) usually predicts that pulsation modes should be excited in bands of Δk modes in radial order.

It is the a posteriori analysis of the multiplet data, interpreted as rotational splitting, that gives us the most confidence in the validity of the inferred seismic model, however. To this end, the values of the first-order solid body rotation coefficient C_{kl} of the modes computed in the optimal model have been listed in Table 2. (The values of the kinetic energy have also been tabulated, but this is just for completeness and to relate to Subsection 4.4.) The interesting aspect is that these values are significantly different; for example $C_{kl} = 0.492$ for the $l = 1$, $k = 1$ mode (its corresponding observed mode shows a fine structure triplet), but $C_{kl} = 0.084$ for the $l = 2$, $k = 2$ mode (its corresponding observed mode shows a fine structure doublet). This means that significantly different frequency splittings should be observed from one multiplet to another, thus providing a robust test of the inferred mode identification.

The values of the C_{kl} coefficients for the five observed modes showing fine structure have been reported in Table 1 (5th column). Using equation (17), and remembering that $\sigma = 2\pi\nu$ and $\Omega = 2\pi/P_{\rm rot}$, we computed estimates of the rotation period of GD 165 for each of the multiplets as indicated in the 6th column of the table. The quoted uncertainties come solely from the uncertainties in the values of the frequency splittings between adjacent multiplet components. Table 1 indicates a most remarkable internal consistency between the five estimates of $P_{\rm rot}$ thus obtained. The rms average gives a remarkably accurate estimate ($\sim$1%) of 57.09$\pm$0.57 h for the rotation period of GD 165, the most reliable value ever obtained for a ZZ Ceti star.

Figure 30 nicely summarizes the excellent agreement that exists between 12 of the observed frequencies and the split frequencies coming out of the assigned modes in the optimal model assuming solid body rotation with a period of 57.09$\pm$0.57 h. Of course, to produce this figure, we have shifted the central components of the observed and theoretical multiplets to the same zero value, as the optimal fit (see Table 2) does not reproduce the frequencies at a perfect level of accuracy. For a given theoretical multiplet, the central component was fixed at zero with no uncertainty, and the $m \neq 0$ components were computed using equation (19) and the uncertainty of 0.57 h on the assumed rotation period. For their part, the uncertainties on the individual values of the 12 frequencies come from Table 1. It is *most* improbable that the agreement between the values of the frequency spacings between the two sets of values can be due to chance. This excellent agreement must rather be seen as a solid proof of the basic validity of the seismic model obtained for GD 165.

It is interesting to examine the rotation kernel of each of the five modes identified with observed multiplets. This is shown in Figure 31 which clearly illustrates that these modes are sensitive to rotation only in the outer part of the stellar model, which contains little mass. Hence, our results that suggest that GD 165 rotates rigidly have to be interpreted in the light of this obser-

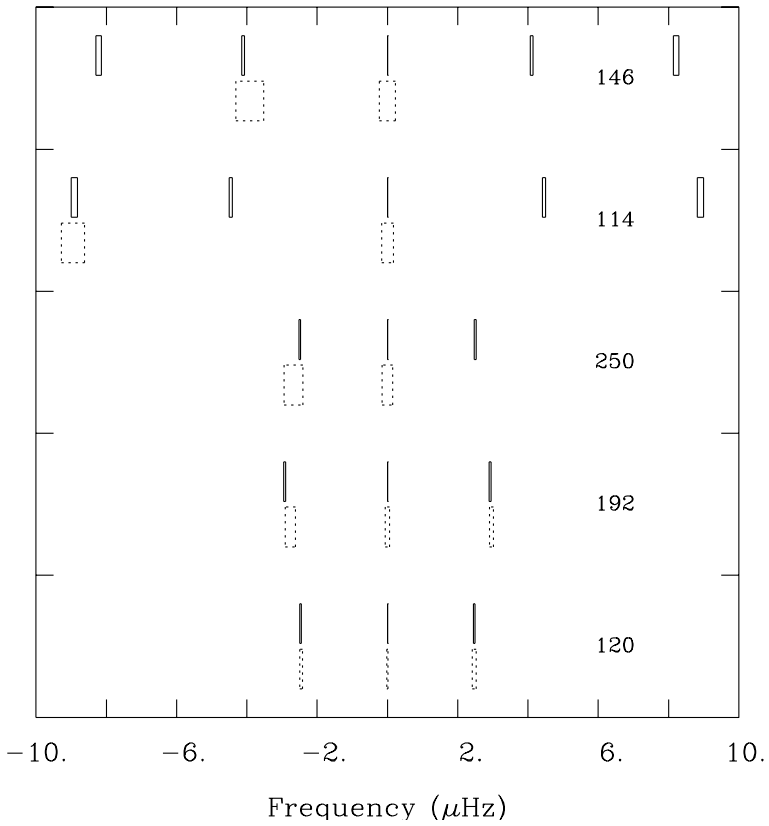

Fig. 30. Comparison of the observed multiplet structures with those predicted on the basis of the optimal model assuming a solid body rotation with a period of 57.09±0.57 h.

vation: the internal rotation profile is only probed adequately in the outer $\sim$ 30% of the radius of GD 165 with the modes available. One could not exclude for example that the inner regions rotate at different rates than the outer part. This limitation is a characteristic of very degenerate white dwarfs such as ZZ Ceti stars. In contrast, as shown by [8], the rotation kernels for g-modes are rather uniformly distributed from the center to the surface in very hot white dwarfs of the GW Vir type. This allows the probing of the entire rotation profile in these objects. Very much like the case of the outward migration of the weight function of an eigenfrequency as discussed above in the context of Figure 9, cooling also pushes the rotation kernel of a given g-mode toward the outer layers as a result of the general increase of the state of degeneracy in the interior and the concomitant decrease of the Brunt-Väisälä frequency.

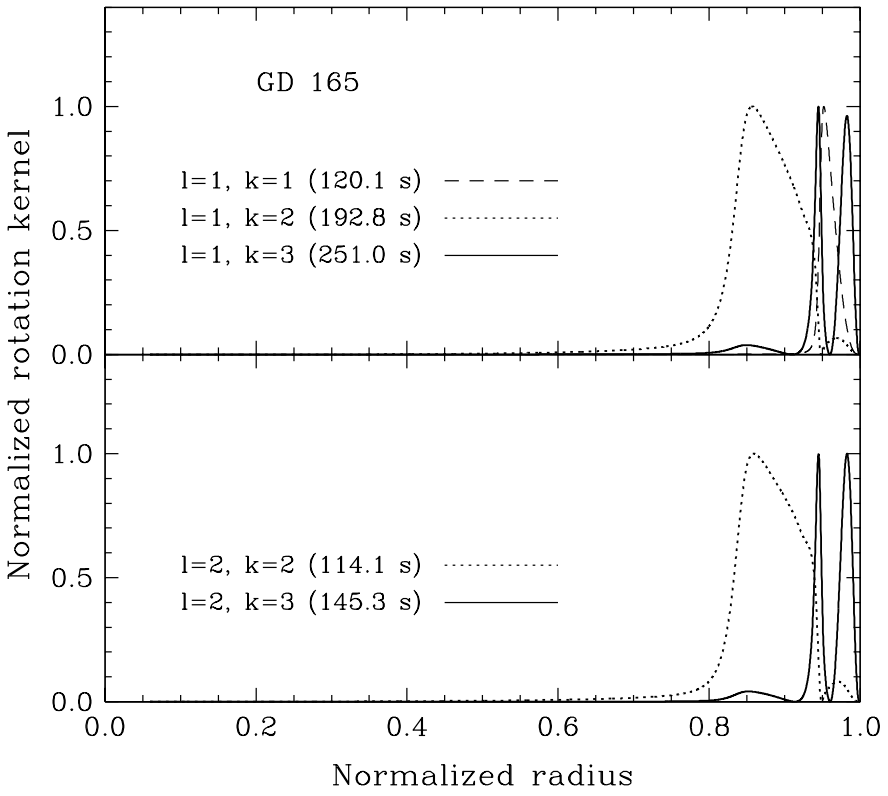

Fig. 31. Normalized rotation kernel for each of the five modes identified in the optimal model of GD 165 and associated with observed rotationally-split multiplets.

7.3 Nonadiabatic considerations and the optimal model

It is instructive to analyze the optimal model with a nonadiabatic pulsation code to verify if the modes identified with the observed ones are indeed predicted to be unstable. This provides a very important consistency check and, if successful, adds credibility to the inferred seismic model. As stated previously, the periods of the low-order modes found in GD 165 are quite insensitive to the choice of the convective efficiency that has been made in the model building phase. However, the question of the stability of the modes *does* depend sensitively on the choice of the assumed convective efficiency as was discussed around Figure 23 above. The models that were built in the search exercise used the ML2/α=1.0 version of convection which, not by accident, is the version that was "calibrated" by matching the theoretical with the empirical blue edge of the ZZ Ceti instability strip. This calibration is based on the assumption that the perturbation of the convective flux adjusts instantaneously, which is

a reasonable hypothesis near the blue edge of the strip since the convective turnover timescale there is much smaller than the pulsation periods of interest as pointed out in Subsection 6.3.

Table 3. Nonadiabatic properties of the optimal model of GD 165

l	k	P(s)	σ_R(rad/s)	σ_I(rad/s)	τ_e(yr)
1	1	120.143	5.23×10^{-2}	-2.60×10^{-13}	1.23×10^{5}
1	2	192.770	3.53×10^{-2}	-2.12×10^{-13}	1.50×10^{5}
1	3	251.015	2.50×10^{-2}	-9.72×10^{-11}	3.28×10^{2}
2	1	69.406	9.05×10^{-2}	-2.88×10^{-13}	1.11×10^{5}
2	2	114.061	5.51×10^{-2}	-3.24×10^{-13}	9.82×10^{4}
2	3	145.281	4.33×10^{-2}	-1.11×10^{-10}	2.86×10^{2}
2	4	168.008	3.74×10^{-2}	-3.38×10^{-10}	9.41×10^{1}
2	5	205.824	3.05×10^{-2}	-3.30×10^{-9}	9.67×10^{0}
2	6	224.865	2.79×10^{-2}	-6.13×10^{-9}	5.20×10^{0}
2	7	239.894	2.61×10^{-2}	-9.75×10^{-9}	3.27×10^{0}
2	8	269.077	2.34×10^{-2}	-6.67×10^{-8}	4.78×10^{-1}

Table 3 summarizes some of the results obtained with the Montréal nonadiabatic pulsation code. The modes identified with the observed ones in GD 165 are indeed excited in the optimal model. In fact, all dipole modes with radial order between $k = 1$ and $k = 22$, and all quadrupole modes with radial order between $k = 1$ and $k = 25$ are predicted to be driven in the optimal model, as well as many low-order p-modes, including radial modes. This is a fairly common situation in nonadiabatic linear physics which tends to predict wider bands of excited periods than those observed.[7] But the important test is that the modes in the optimal model assigned to the observed modes in GD 165 are indeed expected to be excited. Doubts could justifiably have been cast on the credibility of the optimal model if it had failed this test.

The table also indicates that, for all modes, $|\sigma_R| \gg |\sigma_I|$, which is consistent with an earlier remark made above. In addition, the e-folding timescales listed there are all much smaller than the evolutionary timescale of GD 165, meaning that the predicted unstable modes have plenty of time to develop an observable amplitude. And indeed, it takes $1-3\times10^8$ yr for a typical H-atmosphere white dwarf to cross the ZZ Ceti instability strip.

[7] Some researchers prefer to refer to "unstable" modes as those predicted to be driven, and to "excited" modes as those actually observed to have grown a detectable amplitude in a real star. Given that linear nonadiabatic theory does not specify which of the unstable modes will become an observable mode, this point of view merits consideration.

7.4 The inferred properties of GD 165

The primary quantities derived from our asteroseismological exercise for GD 165 are the effective temperature $T_{\rm eff}$ = 12,055±1370 K, the surface gravity $\log g$ = 8.045±0.070, the fractional mass of the He mantle $\log \Delta M({\rm He})/M$ = −1.63±0.12, and the fractional mass of the H outer envelope $\log \Delta M({\rm H})/M$ = −4.14±0.22. The uncertainties on the derived parameters have been estimated using the method described in [5]. Given the particular mass-radius relationship that white dwarfs must obey, a star with these parameters and with a pure C core must have a mass M = 0.633±0.034 $M_\odot$ and a radius of R = 0.0125±0.0007 $R_\odot$. This assumes that the uncertainties on the gravity are shared equally by the mass and the radius. Knowing the radius and the effective temperature, the luminosity follows, $L = 3.0 \pm 1.7 \times 10^{-3}$ $L_\odot$. The relatively large uncertainty associated with L is mostly due to the uncertain effective temperature, which is a consequence of the relatively low sensitivity of the pulsation periods on that parameter as can be appreciated from the shape of the S^2 contour curves in Figure 28 above. Furthermore, and in conjunction with an appropriate model atmosphere based on the ML2/α=1.0 version of the mixing-length theory, the absolute magnitude in the V band is obtained as $M_V(T_{\rm eff}, M, g)$ = 11.73±0.46. The latter result is combined with the apparent magnitude V = 14.32 ± 0.01, leading to an estimate of the distance to GD 165 of d = 33.0±7.1 pc, quite close to the best available astrometric value of d = 31.5 ± 2.5 pc ([25]). The rotation period of GD 165 is inferred to be 57.09±0.57 h, leading to a negligible equatorial velocity of $V_{\rm eq}$ = 0.267±0.017 km s^{-1}.

As discussed above, the periods observed in GD 165 are insensitive to the core composition and the choice of the convective efficiency assumed to build the model, so no useful inference can be made on the basis of the period data for those two parameters. However, nonadiabatic calculations based on the "calibrated" ML2/α=1.0 version of the mixing-length theory and applied to the seismic model of GD 165 indicate that the observed pulsation modes are indeed expected to be excited. In addition, [3] have shown that GD 165 is currently still undergoing element separation and that the standard assumption of diffusive equilibrium is unjustified, at least for this star. This is an interesting piece of information about GD 165 and relates directly to the *actual* shapes of the chemical profiles in the transition zones in this cooling white dwarf. Additional inferences can also be made using after-the-fact full evolutionary calculations built on the basis of the derived structural parameters. For instance, if GD 165 has a pure C core, its cooling age would be 4.15×10^8 yr, while it would be equal to 3.64×10^8 yr if it has a pure O core. Presumably, its true age is sandwiched in between those two values as a typical white dwarf with a mass of $\simeq 0.63$ $M_\odot$ is expected to have a C/O core (but in unknown proportions). These extra evolutionary calculations also lead to the prediction that the rate of period change of the 120.356 s mode in GD 165 (the largest amplitude mode in that star) should be $dP/dt = 6.8 \times 10^{-16}$ s/s if the core

is made of pure carbon, and of $dP/dt = 7.8 \times 10^{-16}$ s/s if the core is made of pure oxygen. Unfortunately, due to the smallness of these values, it is doubtful that this will ever be measured, but the prediction is made.

8 Conclusion

We have tried in this book chapter to provide an original approach to white dwarf asteroseismology. In particular, given the recent availability of two very detailed reviews on the properties of pulsating white dwarfs ([17]; [44]), we have refrained from providing what would have been, at best, a detailed summary of these reviews. In this context, the long reference lists found in [17] and in [44] remain precious material.

In the spirit of this book, we have instead concentrated on a pedagogical approach, with the aims of describing the most basic aspects of asteroseismology as applied to white dwarf stars. We first established several fundamental notions of pulsation theory using pulsating white dwarfs as examples. In this process, we developed and used original material to a large extent. Our demonstration culminated with the example of a successful asteroseismological analysis carried out for the ZZ Ceti star GD 165. This example underlines, in a nice way we believe, the power of asteroseismology in its "forward approach" version, a method that has been underexploited in our view. We hope that our efforts will be useful to the general reader.

Acknowledgments: We are most grateful to Hideyuki Saio and Jagoda Daszyńska-Daszkiewicz for their careful reading of this manuscript and their useful suggestions. This work was supported in part by the Natural Sciences and Engineering Research Council of Canada. G.F. also acknowledges the contribution of the Canada Research Chair Program.

References

1. Arras, P., Townsley, D.M., & Bildsten, L. 2006, ApJ, 643, L119
2. Bergeron, P. et al. 1993, AJ, 106, 1987
3. Brassard, P., & Fontaine, G. 2006, Mem. Soc. Astron. Ita., 77, 439
4. Brassard, P. et al. 1992, ApJS, 80, 369
5. Brassard, P. et al. 2001, ApJ, 563, 1013
6. Brickhill, A.J. 1983, MNRAS, 204, 537
7. Chandrasekhar, S. 1964, ApJ, 139, 644
8. Charpinet, S., Fontaine, G., & Brassard, P. 2009, Nature, 461, 501
9. Charpinet, S. et al. 1997, ApJ, 489, L149
10. Charpinet, S. et al. 2005, A&A, 437, 575
11. Charpinet, S. et al. 2008, A&A, 489, 377
12. Córsico, A. et al. 2009, ApJ, 701, 1008
13. Dufour, P. et al. 2007, Nature, 450, 522

14. Dufour, P. et al. 2011, ApJ, 733, L19
15. Dupret, M.-A. et al. 2008, Journal of Physics Conferences Series, 118, 012051
16. Dziembowski, W. 1971, Acta Astr., 21, 289
17. Fontaine, G., & Brassard, P. 2008, PASP, 120, 1043
18. Fontaine, G. et al. 1993, in White Dwarfs: Advances in Observations and Theory, Proc. 8th European Workshop on White Dwarfs, ed. M.A. Barstow, NATO ASI Series, 403, 485
19. Fontaine, G. et al. 2008, A&A, 486, L39
20. Gianninas, A. et al. 2010, ApJ, 720, 581
21. Green, E.M. et al. 2003, ApJ, 583, L31
22. Handler, G. 1998, A&A, 339, 170
23. Hansen, C.J., Winget, D.E., & Kawaler, S.D. 1985, ApJ, 297, 544
24. Kilkenny, D. et al. 1997, MNRAS, 285, 640.
25. Kirkpatrick, J.D. 2005 Ann. Rev. A&A, 43, 195
26. Landolt, A.U., 1968, ApJ, 153, 151
27. Lynden-Bell, D., & Ostriker, J.P. 1967, MNRAS, 136, 293
28. McGraw, J.T. et al. 1979, in IAU Colloquium 53, White Dwarfs and Variable Degenerate Dwarfs, ed. H.M. Van Horn & V. Weidemann (Rochester, NY: U. Rochester Press), 377
29. Montgomery, M.H., & O'Donoghue, D. 1999, Delta Scuti Star Newsletter, No. 13
30. Montgomery, M.H. et al. 2008, ApJ, 678, L51
31. Quirion, P.-O., Fontaine, G., & Brassard, P. 2004, ApJ, 610, 436
32. Quirion, P.-O., Fontaine, G., & Brassard, P. 2007, ApJS, 171, 219
33. Quirion, P.-O. et al. 2008, in ASP Conf. Ser. 391, Hydrogen-Deficient Stars, ed. K. Werner & T. Rauch (San Francisco: ASP), 183
34. Randall, S.K. et al. 2005, ApJS, 161, 456
35. Randall, S.K. et al. 2011, ApJ, 737, L27
36. Robinson, E.L., Kepler, S.O., & Nather, R.N. 1982, ApJ, 259, 219
37. Saio, H. 1996, in ASP Conf. Ser. 96, Hydrogen-Deficient Stars, ed. C.S. Jeffery, U. Heber & S. Moehler (San Francisco: ASP), 361
38. Saio, H., Winget, D.E., & Robinson, E.L., 1983, ApJ, 265, 982
39. Silvotti, R. et al. 2011, A&A, 525, 64
40. Unno, W. et al. 1989, Nonradial Oscillations of Stars, Tokyo University Press
41. Van Grootel, V. et al. 2008, A&A, 483, 875
42. Van Grootel, V. et al. 2012, A&A, 593, 87
43. van Zyl, L. et al. 2000, Baltic Astronomy, 9, 231
44. Winget, D.E., & Kepler, S.O. 2008, Ann. Rev. A&A, 46, 157
45. Winget, D.E. et al. 1982, ApJ, 262, L11
46. Woudt, P.A. et al. 2006, MNRAS, 371, 1497